The Asian tropopause aerosol layer within the 2017 monsoon anticyclone: Microphysical properties derived from aircraft-borne in situ measurements

Christoph Mahnke[1,*], Ralf Weigel[2], Francesco Cairo[3], Jean-Paul Vernier[4,5], Armin Afchine[6], Martina Krämer[6,2], Valentin Mitev[7], Renaud Matthey[8], Silvia Viciani[9], Francesco D'Amato[9], Felix Ploeger[6], Terry Deshler[10], and Stephan Borrmann[1,2]

[1]Particle Chemistry Department, Max Planck Institute for Chemistry, Mainz, Germany
[2]Institute for Atmospheric Physics, Johannes Gutenberg University, Mainz, Germany
[3]Institute of Atmospheric Sciences and Climate, ISAC-CNR, Rome, Italy
[4]National Institute of Aerospace, Hampton, Virginia, USA
[5]NASA Langley Research Center, Hampton, Virginia, USA
[6]Institute of Energy and Climate Research - IEK7, Forschungszentrum Jülich, Jülich, Germany
[7]Centre Suisse d'Electronique et de Microtechnique, CSEM SA, Neuchâtel, Switzerland
[8]Institut de Physique, Université de Neuchâtel, Neuchâtel, Switzerland
[9]National Institute of Optics, CNR-INO, Sesto Fiorentino, Italy
[10]Department of Atmospheric Science, University of Wyoming, Laramie, Wyoming, USA
[*]now at: Institute of Energy and Climate Research - IEK8, Forschungszentrum Jülich, Jülich, Germany

Correspondence: Christoph Mahnke (c.mahnke@fz-juelich.de)

Abstract. The Asian summer monsoon is an effective pathway for aerosol particles and precursors from the planetary boundary layer over Central, South, and East Asia into the upper troposphere and lower stratosphere. An enhancement of aerosol particles within the Asian monsoon anticyclone (AMA) has been observed by satellites, called the Asian tropopause aerosol layer (ATAL). We discuss airborne in situ and remote sensing observations of aerosol microphysical properties conducted during the 2017 StratoClim field campaign within the AMA region. The aerosol particle measurements aboard the high-altitude research aircraft M55 Geophysica (maximum altitude reached: ~ 20.5 km) were conducted with a modified Ultra-High Sensitivity Aerosol Spectrometer-Airborne (UHSAS-A; particle diameter detection range: 65 nm to 1 µm), the COndensation PArticle counting System (COPAS, detecting total concentrations of submicrometer sized particles), and the New Ice eXpEriment – Cloud and Aerosol Spectrometer with Detection of POLarization (NIXE-CAS-DPOL). In the COPAS and UHSAS-A vertical particle mixing ratio (PMR) profiles and the size distribution profiles (for number, surface area, and volume concentration), the ATAL is evident as a distinct layer between ~ 370 K and 420 K potential temperature (Θ). Within the ATAL, the maximum detected PMR (from the median profiles) were ~ 700 mg^{-1} for particle diameters between 65 nm to 1 µm (UHSAS-A) and higher than 2500 mg^{-1} for diameters larger than 10 nm (COPAS). These values are up to two times higher than previously found at similar altitudes in other tropical locations. The difference between the PMR profiles measured by the UHSAS-A and the COPAS indicate that the region below the ATAL at Θ levels from 350 to 370 K is influenced by the nucleation of aerosol particles (diameter < 65 nm). We provide detailed analyses of the vertical distribution of the aerosol particle size distributions and the PMR and compare these with previous tropical and extratropical measurements. The backscatter ratio

(BR) was calculated based on the in situ measured aerosol particle size distributions. The resulting data set was compared with the vertical profiles of the BR detected by the Multiwavelength Aerosol Scatterometer (MAS) and an airborne Miniature Aerosol Lidar (MAL) aboard the M55 Geophysica and by the satellite-borne Cloud-Aerosol Lidar with Orthogonal Polarization (CALIOP). The data of all four methods largely agree with each other, showing enhanced values of BR in the altitude range of the ATAL (between ~ 15 km and 18.5 km) with a maximum at 17.5 km altitude. By means of the AMA-centered equivalent latitude calculated from meteorological reanalysis data it is shown that such enhanced values of the BR larger 1.1 could only be observed within the confinement of the AMA.

1 Introduction

During the Asian summer monsoon (ASM) the upper troposphere / lower stratosphere (UT/LS) over the Indian subcontinent is strongly influenced by the Asian monsoon anticyclone (AMA). Inside the AMA, the ATAL (Asian tropopause aerosol layer) was discovered from faint signals of satellite-borne lidar measurements (Vernier et al. (2009); Vernier et al. (2011); Vernier et al. (2018)). Its vertical extent typically ranges from 14 to 18 km altitude roughly corresponding to 360 K until 420 K potential temperature levels, respectively. The AMA develops periodically during the summer of the northern hemisphere (Park et al. (2007)), covering a vertical extent from about 12 to 18 km altitude and it has its maximum strength at 17 to 18 km, around the local tropopause (Ploeger et al. (2015); Brunamonti et al. (2018)). With the large variability in its horizontal extent, the AMA covers longitudes from Northeastern Africa to East Asia (Pan et al. (2016); Vogel et al. (2019)). The dynamic processes associated with the AMA provide the setting for an effective vertical transport of trace substances from the lower troposphere accompanied with a certain level of accumulation within the anticyclone. These processes affect the composition of trace gases, particle precursor gases and aerosol particles in all levels of the UT/LS with varying intensities (Randel and Park (2006); Park et al. (2009) Randel and Jensen (2013); Vogel et al. (2015); Pan et al. (2016); Bucci et al. (2020)).

The AMA is a prominent feature with a closed, quasi-rotational circulation in the UT/LS, which is confined by a westerly jet stream in the mid-latitudes and an easterly jet stream in the tropics (Dunkerton (1995); Pan et al. (2016); Brunamonti et al. (2018)). Associated with the AMA are large convective systems during monsoon times which provide rapid vertical transport routes for trace substances, aerosol precursors, and aerosol particles from the boundary layer to the altitude levels of the AMA, the tropical tropopause layer (TTL), and the lower stratosphere (Fueglistaler et al. (2009)). The lifted material includes anthropogenic releases from ground level pollution such as ammonia which forms ammonium nitrate particles in the troposphere (Höpfner et al. (2019); Wang et al. (2020)), which can impact ice cloud formation in the Asian monsoon upper troposphere (Wagner et al. (2020)). The TTL, which in this area extends over an altitude range of about 14 to 18 km, acts as a "gateway to the stratosphere" (Fueglistaler et al. (2009)), because from here, air can be transported into the lower stratosphere via diabatic ascent (Garny and Randel (2016)). With the transport of climate-relevant natural and anthropogenic trace gases, water vapor, and aerosol particles into the stratosphere, also precursor gases enter the UT/LS, which can lead or contribute to the formation of new particles from the gas phase (new particle formation, NPF) (Brock et al. (1995); Weigel et al. (2011); Williamson et al. (2019)). Asia is currently one of the regions with the highest emission of atmospheric sulfur worldwide.

Therefore, the vertical transport of these sulfur-containing aerosol particles and particle precursor gases, through the high-reaching convection of the ASM, can influence the chemical balance of the stratosphere and the climate (Vernier et al. (2011); Kremser et al. (2016)). This was initially suggested as cause for the ATAL (Vernier et al. (2011); Neely et al. (2014); Yu et al. (2015)), however, Höpfner et al. (2019) demonstrated that ammonium nitrate formed from gaseous ammonia and nitric acid in the higher troposphere is an important if not the dominant component of the ATAL aerosol. Furthermore, model analysis (with the GEOS-Chem transport model) by Fairlie et al. (2020) indicate the dominance of regional anthropogenic emissions of particle precursors like sulfate, nitrate, and ammonia, but also aerosol particles (e.g. like primary organic aerosol) from China and the Indian subcontinent to aerosol concentrations in the ATAL.

For a more detailed analysis of these processes, airborne measurements of the microphysical properties of aerosol particles are discussed in this study. These measurements were conducted during the 2017 StratoClim field campaign at the time of the ASM. In this paper we examine the vertical distribution of the submicron aerosol particle mixing ratio and the aerosol particle size distributions within the AMA region. Balloon-borne in situ aerosol backscatter measurements from Vernier et al. (2015), Yu et al. (2017), Brunamonti et al. (2018), and Vernier et al. (2018) confirmed the enhanced aerosol signal observed by Vernier et al. (2011) since 2006. In order to relate their observations with our in situ observations obtained during StratoClim 2017, we calculate the theoretically expected backscatter ratio based on our in situ measured aerosol particle size distributions. With a focus on the ATAL region, we compare these results with observations from the satellite-borne Cloud-Aerosol Lidar with Orthogonal Polarization (CALIOP) (Winker et al. (2010); Vernier et al. (2011)), the airborne backscatter probe MAS (Sec. 3.4) and the airborne lidar MAL (Sec. 3.5) during StratoClim 2017.

2 The StratoClim field campaigns in the Mediterranean (2016) and the Asian summer monsoon region (2017)

The 2017 StratoClim (Stratospheric and upper tropospheric processes for better climate prediction) field campaign took place in July and August in Kathmandu (Nepal). The goal of StratoClim (www.stratoclim.org) was to gain a better understanding of the key processes in the upper troposphere and stratosphere of the ASM region in order to better assess the effects on climate change and stratospheric trace gases including ozone. The StratoClim project comprised a measurement campaign with aircraft-borne and balloon-borne measurements (launched at tropical ground stations at different locations on the Indian subcontinent), satellite-based observations and process-related, regional and global model studies. The choice of Kathmandu as a base for the M55 Geophysica research aircraft (Borrmann et al. (1995); Stefanutti et al. (1999)) allowed measurements to be carried over Nepal, India, Bangladesh and the Bay of Bengal within the AMA. The M55 Geophysica was equipped with extensive instrumentation to measure aerosol and cloud microphysics, aerosol chemistry, trace gases, radiation, and other basic meteorological parameters. The 2017 StratoClim measurement campaign included eight mission flights outbound from Kathmandu (Nepal) Tribhuvan International Airport (TIA) with a total flight time of about 31 hours (Fig. 1). Out of the eight measurement flights, three (KTM2, KTM4, and KTM5) took place exclusively in the Nepalese airspace. These flights were carried out along an axis parallel to the Himalayan mountains over almost the entire east-west extension of Nepal. Three further measurement flights (KTM3, KTM7, and KTM8) were over northeastern India. These flight patterns allowed studying

the horizontal structure of the AMA over large parts of its north-south extension. Bucci et al. (2020) showed that the first half of the StratoClim 2017 campaign period was less affected by regional convective activity compared to the second half, allowing to observe the ATAL under "dry" conditions (flights KTM1 to KTM4) and under convective influence (flights KTM5 to KTM8).

In this study, we also included measurements from the first phase of the StratoClim project which took place in 2016 at Kalamata, Greece (37° N, 22° E). During this campaign phase three flights between 33° N - 41° N and 23° E - 31° E, reaching up to 20 km altitude were conducted in the Mediterranean region (30 August, 1 September, and 6 September) using the M55 Geophysica. The geographical extend and the location of these flights relative to the strong subtropical potential vorticity (PV) gradient (von Hobe et al. (2021)) indicates that these flights took place at the edge of the extratropics and the tropics. The results from these (here refereed to as) extratropical aerosol measurements are juxtaposed to the tropical data from the ASM during StratoClim 2017.

3 Instrumentation on the M55 Geophysica high-altitude research aircraft

The main instrument used for the measurements discussed in this study is the aerosol spectrometer UHSAS-A (see Sec. 3.1). Besides the UHSAS-A, in situ and remote sensing instruments aboard the M55 Geophysica were included for the analyses discussed in this study: The in situ particle detectors COPAS (Sec. 3.2) and NIXE-CAS (Sec. 3.3), the backscatter probe MAS (Sec. 3.4), the airborne lidar MAL (Sec. 3.5), and the carbon monoxide instrument COLD2 (Sec. 3.6). The meteorological parameters and the avionic data from the M55 Geophysica is provided by the Unit for Connection with Scientific Equipment (UCSE; Sokolov and Lepuchov (1998)). The potential temperature (Θ) is calculated from the UCSE-based temperature and pressure data as defined by the World Meteorological Organization (WMO (1966)). For the given vertical temperature and pressure distribution and for the Θ range covered during StratoClim 2017 (up to ~ 477 K), the WMO-compliant Θ values do not deviate by more than ~ 1 K from the results according to the recently reassessed Θ calculation (Baumgartner et al. (2020)).

3.1 The UHSAS-A

The Ultra-High Sensitivity Aerosol Spectrometer Airborne (UHSAS-A) is the underwing version of the UHSAS (Cai et al. (2008)), a laser-based aerosol spectrometer designed and manufactured by Droplet Measurement Technologies (DMT, Boulder, Colorado, USA). It is designed for airborne operation at altitudes of up to 12 km and is able to measure aerosol particle number size distributions in the diameter range from 65 nm to 1 μm at 1 Hz sampling frequency.

For operations at altitudes up to 20 km under tropical, stratospheric ambient conditions aboard the research aircraft M55 Geophysica two major modifications of the commercially available version of the UHSAS-A were necessary: integrating a pressure sensor measuring the air pressure in the optical detection cell of the UHSAS-A and installing a new pump system enabling the maintenance of constant system flows even under low stratospheric air pressures. The stability of the sample, sheath, and purge flow was first tested within a low pressure chamber, before the StratoClim 2017 field campaign. This low pressure chamber tests were conducted under air pressure values down to 45 hPa within the UHSAS-A measurement cell.

During the operation aboard the M55 Geophysica the sample, sheath, and purge flow were stable and constant throughout all StratoClim 2017 mission flights (Appendix A1). Additionally, the new dual headed membrane pump system, installed in the UHSAS-A, minimizes the pulsation of the flow within the UHSAS-A measurement cell compared to a single headed membrane pump. The sample flow measurement was characterized as a function of pressure. For this purpose the UHSAS-A was located in the low pressure chamber and connected through a chamber outlet via a high precision needle valve to a reference flow meter (Gilibrator Version 2 by SENSIDYNE; Appendix A1).

Prior to the 2017 StratoClim field campaign the UHSAS-A was calibrated with polystyrene latex spheres (PSL, Thermo Fisher Scientific) with diameters of 102, 147, 296 and 799 nm. During the calibration process the PSL particles were size-selected with a differential mobility analyzer (DMA, TSI 3080 with TSI 3081) to remove doublets and contamination particles (Appendix A2). During the field campaign in Nepal, before every mission flight the calibration of the UHSAS-A was validated with the same PSL calibration standards without the DMA. The uncertainty of the measured number concentration was determined to be lower than 10 % based on laboratory characterization (Appendix A3). This is valid as long as the uncertainty due to counting statistics is also lower than 10 %. For the 1 Hz resolved measurements, this is the case for ambient particle number concentrations larger than 100 cm^{-3}. At ambient particle number concentrations as low as 1 cm^{-3} the data should be averaged over time intervals of about 100 seconds to gain sufficient counting statistics. For a typical number of about 70 particle counts for a sampling interval of 1 second in the ATAL altitude range, this would result in an uncertainty of 12 %. But, due to missing in-line temperature measurements and the wide ambient temperature range during StratoClim (compared to the characterization in the laboratory), the total uncertainty of the UHSAS-A ambient number concentration and particle mixing ratio measurements was estimated to be up to 25 %.

3.2 COPAS

The COndensation PArticle counting System (COPAS) consists of two separate units, each containing two individual condensation particle counters. Three of the condensation particle counters detect aerosol particles with diameters larger than 6 nm, 10 nm, and 15 nm, respectively. Particles with diameters < 1 μm were aspirated with almost 100 % efficiency and transported through the aerosol lines to the detector. The fourth condensation particle counter detects the aerosol particles with diameters larger than 10 nm, which have previously passed through a heated tube section (at 270 °C) of about one meter length. Therefore, this channel detects residual particle cores which are non-volatile at this temperature. The COPAS has been characterized in Weigel et al. (2009) and the application of the heated channel has been adopted for several studies (Curtius et al. (2005); Borrmann et al. (2010); Weigel et al. (2011); Weigel et al. (2014); Weigel et al. (2021a)).

3.3 NIXE-CAS

The New Ice eXpEriment – Cloud and Aerosol Spectrometer with Detection of POLarization (NIXE-CAS-DPOL, here referred to as NIXE-CAS) is part of the New Ice eXpEriment Cloud and Aerosol Particle Spectrometer (NIXE-CAPS) underwing probe. Together with the Cloud Imaging Probe greyscale (NIXE–CIPg), the NIXE-CAPS can measure the particle size distribution for larger aerosol particles as well as cloud particles within a diameter range from 0.61 to 937 μm (Costa et al. (2017)). The overall

measurement uncertainties of the particle number concentrations and the particle sizing are estimated to be approximately 20 % by Costa et al. (2017). More detailed descriptions of the instrument performance and measuring principles are given by Baumgardner et al. (2017). For this study, the lowest size bins of NIXE-CAS (0.61 to 3 µm) provide additional information extending beyond the upper detection limit of the UHSAS-A, as such large aerosol particles potentially influence the derived backscatter ratios.

3.4 MAS

The Multiwavelength Aerosol Scatterometer (MAS) is an elastic backscatter near range lidar that operates at wavelengths of 532 or 1064 nm. It measures the backscatter and the depolarization from cloud and aerosol particles like a remote sensing lidar, but in situ in a range of 3 to 30 m from the aircraft. It is capable of measuring at a time resolution of 5 to 10 seconds, which translates into a horizontal resolution of 1 to 2 km at the M55 Geophysicas cruising speed of about 170 m s^{-1}. The detection limit of the aerosol backscatter coefficient for a single 10 seconds data point is $5 \cdot 10^{-10}$ m^{-1} sr^{-1}. Its technical details and analysis of its measurement performance aboard the M55 Geophysica are discussed in detail by Cairo (2004), Cairo et al. (2011), and Molleker et al. (2014).

3.5 MAL

The Miniature Aerosol Lidar (MAL) aboard the M55 Geophysica is a combination of two identical stand-alone airborne lidar systems, one facing upwards and the other facing downwards. The two microjoule backscatter-depolarization lidar systems operate at a wavelength of 532 nm and are capable of measuring range-resolved backscatter and depolarization profiles along the aircraft flight track, 2 km above and underneath the aircraft. For a 900 second flight interval (at cruising speed of about 170 m s^{-1}) probing an atmospheric layer at 17 km altitude from a distance of $\sim$ 1500 m the detection limit of the aerosol backscatter coefficient is $5 \cdot 10^{-10}$ m^{-1} sr^{-1}. Previous applications of the MAL lidar are discussed in publications by Cairo (2004), Mitev et al. (2014), and Molleker et al. (2014). For the RECONCILE campaign a comparison study between the MAL lidar aboard the M55 Geophysica and the satellite-borne CALIOP lidar was conducted by Mitev et al. (2012).

3.6 COLD2

During the 2017 StratoClim field campaign, the carbon monoxide (CO) mixing ratio was measured in situ by COLD2 (Carbon Oxide Laser Detector 2), the newly improved version of the Cryogenically Operated Laser Diode spectrometer (COLD) aboard the M55 Geophysica. The previous version COLD, based on lead salts laser, operating around liquid nitrogen temperature, was successfully operated during several tropospheric and stratospheric measurement campaigns since 2005 and its functionality is described in detail by Viciani et al. (2008). The present instrument is based on a room temperature quantum cascade laser and updated electronics, with a substantial reduction of weight and dimensions, and no more need of cryogenic fluids. The detection principle of the COLD instruments is based on the tunable diode laser spectroscopy. During the 2017 StratoClim operation, the COLD2 instrument attained an in-flight sensitivity of 1 to 2 ppb with a time resolution of 1 Hz and an accuracy

180 of 3 % (Viciani et al. (2018)). In this study the CO measurements are adopted as tracer for air masses affected by pollution or biomass burning.

4   The vertical distribution of the aerosol particle mixing ratio within the AMA

The identification of transport and nucleation processes (i.e. new particle formation, NPF) of aerosol particles in the UT/LS and their influence on the radiation balance and chemistry of the atmosphere requires the knowledge of the vertical distribution
185 of the aerosol particle properties, such as particle size and number concentration. Figure 2 (a) shows the vertical distribution of the particle mixing ratio (given in number of particles per mg of ambient air) as measured by the UHSAS-A during all research flights of the StratoClim 2017 measurement campaign. The potential temperature (Θ) is used as the vertical coordinate. To ease the recognition of the variability between the individual flights, the measured particle mixing ratios (1 Hz temporal resolution) are marked by data points of different color. In black, the median of the particle mixing ratio of all eight measurement flights,
190 calculated over 5 K potential temperature intervals, is plotted together with the 25% and 75% percentiles as horizontal bars to each median value. To avoid artifacts due to fewer particles at high altitudes the median profile and the the 25% and 75% percentiles were calculated based on the 1 Hz data for $\Theta < 420$ K and based on the resampled 0.1 Hz data set (see red dots in Fig. 3 (a)) for $\Theta > 420$ K. For this we have to assume that above 420 K the atmospheric conditions remain quasi-homogeneous within a 10 second interval (about 1.7 km flight distance). The number of 1 Hz data points included in each 5 K potential
195 temperature interval is indicated in Fig. 2 (b), where each data point implies the measurement of a complete size distribution.

From comparatively high particle mixing ratios (median of about $1500 \, \text{mg}^{-1}$) close to the ground level ($\Theta = 310$ K), the particle mixing ratio decreases by an order of magnitude to about $150 \, \text{mg}^{-1}$ up to a potential temperature of 330 K. As evident from the 1 Hz resolved data, particle mixing ratios of up to $10000 \, \text{mg}^{-1}$ are measured between 310 and 330 K. Up to the Θ level of 345 K, the median particle mixing ratio remains at about $150 \, \text{mg}^{-1}$. The variability of the measurement results
200 increases with Θ, which can be seen from the changes in the deviation of the 25% and 75% percentiles with respect to the median.

From 345 K to 350 K potential temperature, the median value increases to a particle mixing ratio of $300 \, \text{mg}^{-1}$ until it reaches a maximum of $700 \, \text{mg}^{-1}$ at about 365 to 370 K potential temperature. Between 350 and 370 K the 1 Hz data shows a high variability of the particle mixing ratio, both between the different flights, but also when the flights are considered individually.
205 Particle mixing ratios between $6 \, \text{mg}^{-1}$ and over $10000 \, \text{mg}^{-1}$ were measured here. This high variability is also visible in the percentiles. Apart from the variability of the sampled airmasses inherent from the dynamics of the AMA, causes for such variability may also be the occurrence of NPF events, convective outflow, and scavenging by the large persistent convective cloud systems. In these cloud systems many aerosol particles are activated to form condensation nuclei of cloud droplets or get washed out by scavenging, resulting in the observed very low aerosol particle mixing ratios (Croft et al. (2010); Yang et al.
210 (2015)). On the other hand, these strong convective systems can lead to vertical transport of polluted air from the boundary layer, with elevated particle mixing ratios, up to high altitudes. A possible cause for the high particle mixing ratios in this altitude range, and sometimes up to 380 K potential temperature (flight KTM8), can also be NPF from precursor gases. These

precursor gases of natural and anthropogenic origin are also subject to vertical transport by deep convective cloud systems reaching the TTL and cause NPF in case of favorable thermodynamic conditions (Borrmann et al. (2010); Höpfner et al. (2019); Weigel et al. (2021a); Weigel et al. (2021b)). The lapse rate tropopause (LRT in Fig. 2 (a)) during the 2017 campaign period was located between 369 and 396 K at a mean Θ level of about 380 K based on European Centre of Medium-Range Weather Forecasts (ECMWF) ERA-Interim reanalysis data. Above the tropopause region, starting at about 380 K potential temperature, the variability of the particle mixing ratio decreases with increasing Θ.

Up to a potential temperature of 420 K, the median of the particle mixing ratio decreases to about 80 mg^{-1}, except for a local maximum at a potential temperature of 390 K. From there, up to a potential temperature of 440 K, the particle mixing ratio decreases further to a median of about 50 mg^{-1}. Up to about 475 to 480 K, the highest Θ levels reached during the StratoClim 2017 measurement campaign, the median of the particle mixing ratio remains between 40 and 50 mg^{-1}. Especially for potential temperatures larger than 420 K and low particle mixing ratios in the range of 10 to 100 mg^{-1} it is noticeable, that the 1 Hz data points form a vertical and slightly inclined, discrete stripe pattern towards larger particle mixing ratios. This is due to the poor counting statistics of the single 1 Hz data points at these concentrations in combination with the constantly regulated sample flow (of 50 $\mathrm{cm}^3\ \mathrm{min}^{-1}$). However, due to the high number of 1 Hz data points (about 400 to 4000) available for each 5 K interval, even in this Θ range we were able to resample the data set to a temporal resolution of 0.1 Hz, and then calculate robust median values with the given Θ resolution.

For relating these UHSAS-A results to the particle mixing ratios observed in other tropical and subtropical UT/LS regions, two data sets from the tropics as well as two sets from the extratropics were selected. These measurements were conducted with the COPAS instrument (described in Sec. 3.2) during the 2016 StratoClim field campaign in Greece (extratropics) and StratoClim 2017 in Nepal (tropics), as well as air-borne measurements within the tropics and the extratropics, published in Borrmann et al. (2010), and digitized from Fig.1 of the publication by Brock et al. (1995). Figure 3 (a) shows the median profiles of the COPAS measurement series from the 2016 and 2017 StratoClim campaigns together with the median profile from the 2017 StratoClim UHSAS-A data set. In addition to the tropical and extratropical profiles from Brock et al. (1995), Fig. 3 (b) compares the UHSAS-A and COPAS measured profiles from StratoClim 2017 (Nepal) with three further profiles measured by the COPAS instrument within the tropics during the field campaigns SCOUT-AMMA 2006 (West Africa, red line), SCOUT-O3 2005 (Northern Australia, pink dotted line), and TROCCINOX 2005 (Brazil, dark green dotted line), discussed by Borrmann et al. (2010) and Fierli et al. (2011).

In the region of the upper troposphere with potential temperatures between about 350 and 370 K, the median of the particle mixing ratio measured by COPAS during StratoClim 2017 (green line) reaches its maximum of 6000 mg^{-1}. A maximum (particle mixing ratio up to about 6500 mg^{-1}) in this Θ range was also observed by Brock et al. (1995) in the tropical Central Pacific (orange line). The median of the UHSAS-A measurement remains almost constant in this Θ range with significantly lower values of the particle mixing ratio of about 250 mg^{-1}. However, the variability of the particle mixing ratio measured by the UHSAS-A is, as discussed above, very high in this Θ range. The COPAS measurements shown here cover the particle diameter range from about 10 nm to 1 μm, and those of Brock et al. (1995) were from 8 nm to 3 μm, while the UHSAS-A detects aerosol particles in the diameter range from 65 nm to 1 μm. The difference in the particle mixing ratios between the

median values of the COPAS and the UHSAS-A measurements of more than about 5500 mg^{-1} shows, that very small aerosol particles between 10 and 65 nm in diameter dominate the aerosol total particle mixing ratios. This indicates that especially the Θ range between 350 and 370 K is influenced by NPF, what has also been shown by Weigel et al. (2021a) and Weigel et al. (2021b).

During the ASM, between about 370 and 415 K potential temperature, the median profile of the UHSAS-A data (diameter: 65 nm to 1 µm) shows particle mixing ratios that are up to two times higher than the median profile observed by Brock et al. (1995) (diameter: 8 nm to 3 µm) in extratropical regions (see Fig. 3 (b)). The median profile of the COPAS measurement during the StratoClim 2016 measurement campaign in Greece (blue line in Fig. 3 (a)) also shows lower particle mixing ratios than the comparative measurement within the AMA region (green). Compared with the extratropical COPAS measurements from StratoClim 2016, the UHSAS-A vertical profile shows mostly lower particle mixing ratios. However, in contrast to the UHSAS-A, the measurements with the COPAS also include very small aerosol particles starting from 10 nm in diameter (or rather from 6 nm during TROCCINOX 2005). Thus, inside the AMA, higher particle mixing ratios were observed for the size diameter range from 65 nm to 1 µm at altitudes between roughly 370 and 415 K than during similar measurements in the extratropics which include even much smaller particles (starting from 8 nm (Brock et al. (1995))). This enhanced aerosol mixing ratio can be associated with the ATAL discovered by Vernier et al. (2009), who observed the ATAL in about the same altitude range with potential temperatures between 370 and 420 K on the basis of satellite-borne lidar measurements. Figure 3 (b) shows that such a maximum between roughly 340 and 390 K was also observed in the mixing ratios of fine-mode particles obtained from COPAS in other tropical locations (Northern Australia, West Africa, and Brazil; Borrmann et al. (2010)) albeit with significantly lower absolute values than for the AMA region. The increase in particle mixing ratio for altitudes above the 420 K level over West Africa was explained by Borrmann et al. (2010) as influence of the 2006 Soufrière Hills eruption in the Caribbean (also discussed by Prata et al. (2007) and Vernier et al. (2009)). In panel (a) of Fig. 3 a decrease of mixing ratios detected with the UHSAS-A and COPAS from about 170 to 80 mg^{-1} and from 470 to 170 mg^{-1} respectively can be seen between the 410 and 420 K potential temperature levels. The altitude levels of this decrease roughly coincide with the top of the 2017 AMA circulation system (von Hobe et al. (2021)). Aloft, the particle mixing ratios are mainly controlled by the large scale isentropic transport in the lowermost stratosphere and are less influenced by the AMA.

5 The vertical profile of the aerosol particle size distribution within the Asian monsoon anticyclone

Characterizing the ATAL, described by Vernier et al. (2011), requires knowledge about the vertical progression of the aerosol particle size distribution. Within UT/LS altitudes, this is also important for the analysis of NPF events, cloud formation, and transport processes as well as for the calculation of the radiative balance and parameters like aerosol volume concentration (Höpfner et al. (2019)) and aerosol surface area, available for heterogeneous chemical conversion processes.

The results shown here are the first measurements made with an UHSAS-A in the tropical lower stratosphere (up to more than 20 km altitude over the Indian subcontinent). The performance of the modified UHSAS-A (see Sec. 3.1) has been thoroughly tested in laboratory (as described in Appendix A). To put the in situ measurements at altitude into context with some of the other

few available observations, a comparison was made with other optical particle counter measurements of the aerosol particle size distributions from the stratosphere.

For this purpose we chose two measurements conducted with a balloon-borne set-up which continues the series of in situ data described in Deshler et al. (2003), Ward et al. (2014), and Deshler et al. (2019). The comparison measurements were from Hyderabad (India; 17.47 °N, 78.58 °E) in August 2015, also above the ATAL (Vernier et al. (2018)) during the ASM period, and from Laramie (United States of America; 41.32 °N, 105.58 °W) in August 2013. The optical particle counters (LPC; Laser Particle Counter) used for the measurements from Hyderabad and Laramie were operated with a particle diameter detection range from 0.18 to 32 µm and 0.18 to 9 µm, respectively. In both cases total particle concentration measurements were made with a condensation nuclei counter (CNC) with a nominal detection diameter of 20 nm (Campbell and Deshler (2014)), flown in parallel with the LPCs. The resulting particle size distributions are compared in Fig. 4 with the data of the UHSAS-A obtained at the highest flight level (56 hPa pressure level) of the StratoClim mission flight KTM4. This size distribution was combined with the COPAS data for an additional size-bin between 6 and 65 nm. The overlapping size-bin of the NIXE-CAS measurements is shown in blue and agrees with UHSAS-A data well within the uncertainties. In each case the balloon data set (500 m vertical averaging interval) was chosen for which the altitude range corresponded mostly to the flight level of the M55 Geophysica during the UHSAS-A measurements.

For the comparison of these data sets the higher size resolution of the UHSAS-A and the difference in the detection range compared to the balloon-borne instrumentation as well as the temporal and spatial distance between these measurements must be taken into account. Additionally, the size distribution measured during StratoClim 2017 is reported with the bin-limits resulting from the calibration with PSL particles (refractive index m = 1.59; see Appendices A2 and A4), while the balloon-borne measurements were corrected for a refractive index of 1.45.

The ambient total number concentration for the observation from StratoClim 2017 of ~ 9 cm^{-3} is slightly lower compared to the 10 cm^{-3} observed over Hyderabad, but by one third larger than the 6 cm^{-3} measured at Laramie. For a better quantitative comparison of the size distributions the integrated surface area (dS) and volume concentrations (dV) were calculated. For the measurements during StratoClim 2017, these values were calculated using the original bin sizes and the ones recalibrated for a refractive index of m = 1.45. In both cases, for the StratoClim 2017 observation the values for dS ≈ 0.44 µm^{2}cm^{-3} (0.52 µm^{2}cm^{-3} for m = 1.45) and dV ≈ 0.021 µm^{3}cm^{-3} (0.029 µm^{3}cm^{-3} for m = 1.45) are smaller compared to the measurements from Hyderabad and Laramie, with dS ≈ 0.79 µm^{2}cm^{-3} and dV ≈ 0.05 µm^{3}cm^{-3} observed at both locations. Compared with the balloon-borne measurements from Hyderabad, these lower values for total particle number, surface area, and volume concentration observed during StratoClim 2017 also agree with a lower backscatter ratio (BR) signal observed by CALIOP at this altitude during StratoClim 2017. During July and August 2015 CALIOP observed a BR of about 1.07 at ~ 20 km altitude within $\pm$ 5 degree latitude and $\pm$ 30 degree longitude around Hyderabad (Vernier et al. (2018)), while the BR measured by CALIOP during StratoClim 2017 at 20 km was below 1.05 (Sec. 6.2).

Figure 5 shows the vertical profile of the aerosol number size distribution (a), surface area size distribution (b), and volume size distribution (c) measured by the UHSAS-A averaged over the full StratoClim 2017 campaign period. The profiles were averaged with a vertical resolution of 1 K potential temperature. The concentrations for the distributions' diameter bins are

color-coded and normalized according to the bin-widths in terms of dN/dlogDp, dS/dlogDp, and dV/dlogDp. To be able to compare the measured concentrations of the number, surface area, and volume size distributions over the full altitude range, the ambient concentrations have been converted to standard temperature and pressure (STP; $T_0 = 273.15$ K; $p_0 = 1013$ hPa) using the ambient temperature and pressure measurements reported by the UCSE.

320   Starting at a Θ level of 320 K, the profile of the aerosol particle number size distribution (Fig. 5 (a)) has a pronounced maximum at the lower end of the UHSAS-A detection size range (diameter between 65 and 80 nm), together with enhanced number concentrations also for the large aerosol particles, with diameters up to 1 μm. Until about 326 K potential temperature, the size distribution's maximum is located between particle diameters of 70 and 80 nm and the overall number concentration decreases. This is especially the case for particles with a diameter larger than 600 nm. Up to potential temperatures of about

325   350 K the overall shape of the size distribution remains mostly constant. In the Θ range between 350 and 370 K the aerosol size distribution is very variable. It shows high number concentrations also for large particles up to 1 μm in diameter, at the upper detection size-range of the UHSAS-A, and a very pronounced Aitken-mode. Above 370 K potential temperature the main mode of the size distribution broadens and shifts its maximum to diameters of about 100 nm. This shift of the distributions main mode to larger particles is even more prominent in the surface area (Fig. 5 (b)) and volume size distribution (Fig. 5 (c)).

330   This increase in aerosol surface area can have a local effect on heterogeneous chemical processes. Additionally, Yu et al. (2017) reports based on model simulations that these particles spread throughout the entire northern hemispheric lower stratosphere and contribute annually with about 15 % to the stratospheric column aerosol surface area in the northern hemisphere and set a lower limit of the ASM contribution to the global stratospheric aerosol surface area of about 7 %. At about 395 K potential temperature the concentrations, especially for larger particles, begin to decrease. Above 420 K, until the maximum ceiling

335   during StratoClim 2017, the shape of the aerosol size distribution shows only low variability. Altogether, for the 2017 AMA the measured vertical profiles of the aerosol size distributions show the presence of an ATAL feature between approximately 370 and 420 K with the peak of the size distributions in the 80 to 300 nm diameter range.

6   Backscatter properties of the ATAL - results from in situ and remote sensing instruments

     The ATAL was discovered as an enhancement of the newly reanalyzed and cloud-filtered backscatter ratio (BR) signal from

340   the CALIOP lidar aboard the Cloud-Aerosol Lidar and Infrared Pathfinder Satellite Observations (CALIPSO) satellite (Vernier et al. (2009) and Vernier et al. (2011)). Vernier et al. (2015), Yu et al. (2017), Brunamonti et al. (2018), and Vernier et al. (2018) confirmed this enhancement using balloon-borne in situ backscatter and aerosol particle number concentration measurements. To compare with these observations, we calculated the BR based on the in situ measured aerosol particle size distributions from the StratoClim 2017 campaign and compare it with the cloud-filtered CALIOP, MAS (Sec. 3.4), and MAL (Sec. 3.5)

345   measurements for a mostly overlapping time period in 2017.

6.1 Method

For this analysis, all 8 measurement flights from the StratoClim 2017 campaign are divided into segments of 100 seconds. Segments in which cloud particles have been detected by the NIXE-CAS are removed from the data set to be consistent with the cloud filtered CALIOP, MAS, and MAL data sets. To ensure a high vertical resolution, flight segments with ascending or descending rates which result in a potential temperature rise or drop of more than 5 K per 100 seconds of flight time are also removed.

For each remaining 100 second interval an averaged aerosol size distribution was calculated from the UHSAS-A measurements. The size range of this size distributions is extended from 65 nm - 1 μm to 10 nm - 3 μm using measurements conducted by the COPAS (Sec. 3.2) and NIXE-CAS (Sec. 3.3) instruments.

One size-bin from 10 to 65 nm in diameter was calculated by subtraction of the UHSAS-A measured total number concentration (particle diameter range: 65 nm - 1 μm) from the particle number concentration measured by the COPAS N_{10} channel (particle diameter range: 10 nm to about 1 μm) described in Sec. 3.2. The measurements conducted by the NIXE-CAS instrument (see Sec. 3.3) extend the size distribution for large aerosol particles by one size bin with diameters up to 3 μm. This way, as composite, the largest possible aerosol particle diameter range is covered with measurements which can be achieved from all of the Geophysica instruments. One example of this combined 100 s averaged aerosol size distributions is shown in Fig. 6.

The backscatter ratio (BR) is calculated using Eq. 1 with the aerosol backscatter coefficient β_{ap} and the molecular backscatter coefficient β_{mol}.

$$BR = \frac{\beta_{ap} + \beta_{mol}}{\beta_{mol}} \tag{1}$$

For every 100 s - averaged aerosol size distribution the aerosol backscatter coefficient β_{ap} is calculated based on the Mie-theory as comprehensively described in Cairo et al. (2011). Accounting for the aerosol chemical composition (Höpfner et al. (2019) observed the presence of ammonium nitrate particles), these calculations use a refractive index of 1.5 for the size distributions measured within the ATAL altitude region up to 420 K potential temperature. At Θ levels higher than 420 K a refractive index of 1.45 is used, which better reflects the stratospheric aerosol properties. The bin-limits of the UHSAS-A measured size distribution were recalibrated for the respective refractive index prior to the calculation of the backscatter coefficient (see Appendix A4 and Table A1). A sensitivity study (Appendix B) showed that the variation of the calculated aerosol backscatter coefficient is below 50 % for diameter-shifts of the size distribution by $\pm$ 10 % or for a variation of the refractive index by $\pm$ 0.05. Additionally, black carbon particles might alter the result of the backscatter calculations, due to their complex refractive index and the uncertainties for their size representation in the particle size distribution measured by the UHSAS-A (see Appendix A2). Even though the presence of black carbon particles in the ATAL altitudes is enhanced during the ASM season, its contribution to the overall aerosol particle mass concentration (for particle diameters < 2.5 μm) is reported to be only about 1.3 % at the 100 hPa pressure level (Gu et al. (2016)). Also the effect of the particles hygroscopicity on the measured particle sizes and the resulting calculated backscatter compared with the remotely sensed backscatter, which are at ambient relative humidity, can not be ruled out.

To be able to compute the backscatter ratio, the molecular backscatter coefficient β_{mol} for each averaging interval is calculated. Based on Collis and Russell (1976), the simplified method from Cairo et al. (2011) is used together with the temperature and pressure measured by the UCSE system aboard the M55 Geophysica. To be able to compare the resulting BR values with the BR measured by CALIOP, MAS, and MAL, β_{ap} and β_{mol} are calculated using a wavelength of 532 nm.

6.2 Comparison between backscatter ratios obtained from in situ and remote sensing data

For a direct comparison between these in situ aerosol size distribution based BR and the BR measured by the satellite-borne lidar CALIOP, a CALIOP data set is needed that was measured within a comparable time period and about the same geographical region as the StratoClim 2017 flight missions. Over the time period from 5 to 31 August 2017 (no CALIOP data is available in this region for the earlier part of the campaign period) a vertical profile of the BR at a wavelength of 532 nm measured by CALIOP was averaged between 15 to 45 degree North and 70 to 100 degree East (total number of profiles included: 311100). This temporal and horizontal averaging is needed to increase the signal to noise ratio. To be able to detect the ATAL, the CALIOP data set was reanalyzed based on the CALIOP data level 1 V4.10 data set and calibrated between an altitude of 36 to 39 km as previously described by Vernier et al. (2009). During this data processing, backscattering due to ice cloud particles was removed by applying a filter for the volume depolarization ratio within a pixel greater than 5% (Vernier et al. (2011); Vernier et al. (2015)). The vertical profile was then averaged with a vertical resolution of 200 m. Additionally, vertical profiles of the BR at a wavelength of 532 nm measured by the MAS and MAL instruments aboard the M55 Geophysica were averaged over all StratoClim 2017 flight missions. Like for the CALIOP data set a cloud-filter was applied to the MAS and MAL data sets. This filter excludes datapoints with a depolarization ratio greater than 5% and BR values greater than 1.3 for the MAS and greater than 1.4 for the MAL.

Figure 7 shows the averaged CALIOP BR profile represented by the red line in an altitude range from 11 to 21 km. The BR calculated based on the in situ measured aerosol size distributions for the 100 seconds time segments (described in Sec. 6.1) is shown as blue dots. The blue line is the averaged profile for size distribution based calculated BR with a vertical averaging interval of 500 m and with the standard deviation represented by blue horizontal bars (shown for the MAS, MAL, and CALIOP BR profiles in Fig. A7). The mean BR profiles measured by the MAS and the MAL are given as green and orange lines, respectively.

At altitudes lower than 13.5 km, the size distribution based BR profile shows smaller values than the CALIOP, MAS and MAL profiles. This can be explained by the frequent appearance of clouds in combination with the fast descent and ascent rates of the M55 Geophysica in this altitude range. Considering the selection criteria for the 100 second time segments described in Sec. 6.1, this leads to only a few valid datapoints in this altitude range. Additionally, the flight segments that are not directly associated with clouds could have been affected previously by scavenging of aerosol particles due to in-cloud processes (Croft et al. (2010); Yang et al. (2015)) that have occurred prior to the observations. The local maximum in the BR profile measured by the MAL in this altitude range might also be considered as an artifact from cloud particles that could not be removed from the signal.

Between 13.5 and about 19 km altitude the BR for the 100 second flight segments scatters around the CALIOP, MAS, and MAL mean profiles with values between 1.01 to over 1.17. Above 14 km altitude its mean BR (blue line) increases from 1.06 parallel with the CALIOP profile (red line) to the maximum of the mean BR of more than 1.11 at altitudes between 17 and 17.5 km. Here also CALIOP, MAS, and MAL observed the BR maximum. The aerosol size distribution shown in Fig. 6 was measured in this altitude range at about 17.5 km and a potential temperature level of 385 K. This 100 s - averaged size distribution leads to a calculated BR of about 1.14. Above this maximum the BR mean profile from the size distribution based calculations and the CALIOP measurements decrease mostly in parallel until 19 km altitude. Between 19 and 21 km altitude the BR of both profiles begins to increase again. Here, the profiles measured by the MAS and the MAL instruments show the same behavior with a trend to higher BR values. This increase in BR is consistent with the lower part of the Junge Layer (Junge et al. (1961); Vernier et al. (2015)). Within the overall picture and under consideration of the standard deviation (blue bars), all four independent methods largely agree with each other. This confirms the ATAL as a layer of enhanced BR, while the altitude range of this observed aerosol layer also agrees very well with the ATAL altitudes between about 14 and 18 km, observed by Vernier et al. (2009), Vernier et al. (2011), Vernier et al. (2015), Brunamonti et al. (2018), and Vernier et al. (2018). The regional total sky radiative forcing caused by the ATAL was reported by Vernier et al. (2015) to be around - 0.1 Wm^{-2} since the late 1990s, which corresponds to one third of the reported total radiative forcing (0.3 Wm^{-2}) from the global carbon dioxide increase during the same time period (Vernier et al. (2018)).

6.3 The ATAL's variability during the StratoClim 2017 campaign period

Bucci et al. (2020) characterized the StratoClim 2017 campaign period as less convectively active than typically expected during that time of the ASM. They also showed that the second half of the campaign period was more influenced by convection compared to the first half. For this reason, we take a closer look at the differences in BR within the ATAL's altitude range during the first and the second half of the campaign period. The backscattering of the size distribution based BR values shows the highly variable nature of the ATAL in time and space. This high variability of the ATAL, even on a day by day basis, was also reported by Hanumanthu et al. (2020) from balloon-borne backscatter measurements conducted during the ASM season 2016. In Fig. 8, the mean profiles of the BR derived from the in situ measured size distributions over the full campaign period (blue line), the first four (green dashed line), and the last four (orange dashed line) of the eight StratoClim 2017 flight missions are shown. The mean profile is only displayed as a line if the corresponding altitude interval includes more than one data point (each resulting from a 100 s - averaged size distribution). The red line in Fig. 8 represents the CALIOP BR profile for the same time period as discussed in the previous section (5 to 31 August 2017).

During the first four mission flights up to 17 km the mean profile of the aerosol size distribution based BR stays at values between about 1.07 and 1.08, except for a peak between 14 and 15 km altitude. The BR values of the individual 100 s - segments still scatter widely in this altitude range, leaving the CALIOP mean profile for the time period from 5 to 31 August 2017 well in the range of the standard deviation (green bars). Between 17 and 17.5 km, the mean profile maximum for the first half of the campaign period matches the maximum of the CALIOP measured BR of about 1.09 to 1.1.

445   Due to the more frequent occurrence of convection during the second half of the campaign period, there are fewer cloud free flight segments at altitudes of up to ~ 15 km. But above that altitude the BR calculated based on the in situ measured aerosol size distributions are significantly higher compared to the first four campaign mission flights. Between 16 and 17.5 km altitude its mean profile exceeds the CALIOP BR profile and has a pronounced maximum layer between 17 and 17.5 km altitude. Here, the size distribution based BR mean profile has a maximum BR between 1.16 and 1.17 compared to about 1.09

450   of the CALIOP mean profile (5 to 31 August 2017). In summary, the direct intercomparison between long time averages of the satellite data and small sets of individual research flights generally is a difficult task. For the ATAL in the ASM season of 2017, however, the juxtaposition of the respective measurements shows that the properties derived from the in situ measured particle size distributions can be broadly reconciled with the satellite observations.

6.4   The ATAL's relation to CO and the AMA-centered equivalent latitude

455   The previous section shows that the intensity of the convective influence has an impact on the characteristics of the ATAL, here discussed in terms of the BR. A commonly used tracer for convective influences on the UT/LS region is an enhancement of the CO mixing ratio (Park et al. (2009); Pan et al. (2016)). Here one has to consider the different timescales of the transport and dilution processes of CO within the UT/LS (tens of days) and aerosol related processes like coagulation and cloud scavenging that can have a significant impact within hours. Furthermore, between June 2006 and August 2008 Vernier et al. (2015) observed

460   a seasonal dependence between the enhanced BR (measured by CALIOP between 14 and 18 km altitude) and an enhancement of the mean CO mixing ratio near the 100 hPa pressure level, as detected by the satellite-borne Microwave Limb Sounder (MLS, V2.21). They found that during the investigated time period the aerosol peak in August lagged the CO peak by about one month.

       Figures 9 (a), (b) and (c) show the relationship between the in situ size distribution based aerosols BR (100 s flight segments)

465   and the averaged CO mixing ratio measured by the COLD2 instrument (described in Sec. 3.6) over the full StratoClim 2017 campaign period, and its first and second half, respectively. For both parts of the campaign, values of the BR larger 1.05 are generally associated with CO mixing ratios larger 40 ppb. The flight segments with CO mixing ratios lower than 40 ppb have all been associated with potential temperature levels larger 420 K (color-coded), close or above the top of the AMA caused confinement at about 420 to 440 K (Brunamonti et al. (2018); von Hobe et al. (2021)). However, especially Fig 9 (c) shows

470   that the highest CO mixing ratios are not necessarily correlated with a high BR. The highest values for the BR (larger than 1.14) encountered during the first four flights are accompanied with CO mixing ratios between 70 and 90 ppb and for the last four flights in the range of 50 to 70 ppb.

       Besides the strong convective vertical transport associated with the ASM, another feature of the ATAL should be considered, namely the confinement of its air masses within the AMA. This confinement can lead to an accumulation of aerosol particles

475   and trace gases within the AMA region. One measure to relate the geographical position of our soundings to the position of the AMA core and its edge is the AMA-centered equivalent latitude (EQLAT). The center of the AMA is defined by the lowest values of the potential vorticity (PV) on the 380 K potential temperature level. An equivalent latitude for which 90 degree North corresponds to the center of the AMA was projected for a closed PV contour according to Ploeger et al. (2015). It has to

be noted that the definition of the EQLAT is only valid for a layer of about ± 10 K around the 380 K isentrope, as outside this range PV contours in the AMA region are frequently not closed. Furthermore, Ploeger et al. (2015) found that the edge of the confinement caused by the AMA can be determined from a local maximum in the gradient of PV along the 380 K isentrope, and is on average located at around 65 degree EQLAT. The EQLAT is calculated based on the ECMWF ERA-Interim reanalysis.

Figures 9 (d), (e), and (f) show the raltionship between the EQLAT and the BR (full campaign period, first half and second half, respectively). While there is no direct correlation between the BR and the EQLAT, high values of BR (larger than 1.1) only occur for flight segments with a EQLAT larger 63 degrees, for the first half of the campaign period (Fig. 9 (a)). During the second half of the StratoClim 2017 campaign BR values larger 1.1 were only detected during flight segments with an EQLAT larger 66 degree. This matches well with the edge of the AMAs confinement at about 65 degree EQLAT described by Ploeger et al. (2015). At high Θ levels above about 420 K (blueish colors) the BR values are always lower than 1.05. This shows that during the ASM typically elevated ATAL BR values could only be observed horizontally and vertically within the confinement of the AMA.

7 Conclusions

During the 2017 StratoClim field mission in the Asian summer monsoon (ASM) season, aerosol measurements were performed over Central Asia up to 20 km altitude aboard the research aircraft M55 Geophysica inside and above the Asian monsoon anticyclone (AMA) and the Asian tropopause aerosol layer (ATAL). Here and for the first time, submicrometer sized aerosol size distributions were measured in situ down to 65 nm particle diameter by a modified UHSAS-A optical particle counter. These measurements were conducted in conjunction with condensation particle counters (COPAS), and two near-range remote sensing instruments, MAS and MAL.

The ATAL BR observations by CALIOP during the StratoClim 2017 campaign period, like discussed e.g. by Vernier et al. (2009), Vernier et al. (2011), and Vernier et al. (2018) for previous and recent ASM seasons, were validated by calculating the BR based on the in situ measured aerosol size distributions, as well as the BR directly measured by the MAS and MAL instruments. All of those four independent methods largely agree with each other and can confirm the ATAL as a layer of enhanced BR within an altitude range from 15 to 18.5 km. The maximum of the ATAL BR signal was observed at 17.5 km altitude, consistently by all four methods. The importance of the ATAL for the earths radiative budged was already underlined by Vernier et al. (2015), reporting the regional total sky radiative forcing caused by the ATAL to be around - 0.1 Wm^{-2} since the late 1990s. Furthermore, the in situ measurements show that the ATAL is highly variable in time and space and is not a closed, persistent layer. While there is a seasonal correlation between the CO mixing ratio and the ATAL (Vernier et al. (2015)), no direct correlation on the smaller scale, between co-located in situ measurements of the CO mixing ratio and the size distribution based BR, could be found. But, values of BR that are typically elevated within the ATAL could only be observed for CO mixing ratios larger than 40 to 50 ppb. This is also consistent with the observations, that during the StratoClim 2017 campaign period enhanced BR values could only be observed within the confinement of the AMA at a equivalent latitudes (EQLAT) larger than 63 degree and below its top of confinement (at about 420 K potential temperature). This regional limitation of the ATAL with

respect to the dynamics of the AMA is in good agreement with the horizontal (Ploeger et al. (2015)) and vertical (von Hobe et al. (2021)) limitations of the AMA-caused confinement.

From the experimental perspective the ATAL is a fairly elusive, highly variable layer situated between approximately 370 K and 420 K potential temperature or about 15 km to 18.5 km altitude. Its lower part is close to –if not still inside- the highest region of convective outflows, while its upper part can be found at tropopause levels (between 369 K and 396 K during StratoClim 2017) or slightly above. Thus the aerosol of the upper ATAL part is subject to very slow vertical ascent (with rates of about 1 K potential temperature per day, reported by Vogel et al. (2019) and von Hobe et al. (2021)). At the same time, the lower part of the ATAL can be affected by rapid turbulent mixing which provides precursor gases and aerosols originating from the lower troposphere. In this complex dynamical setting microphysical processes like new particle formation (NPF), aging by coagulation and condensational growth, and removal by scavenging act on the aerosol. The vertical profile of the measured aerosol particle size distributions in combination with the vertical profiles of the particle mixing ratios from the UHSAS-A and COPAS show a pronounced Aitken-mode between the 350 and 370 K potential temperature levels, i.e. beneath the lower edge of the ATAL. With increasing altitude, the aerosol size distribution's main mode shifts towards the accumulation mode. This goes along with an increase in aerosol surface area, which might have a local effect on heterogeneous chemical processes and additionally contributes to the global stratospheric aerosol surface area (Yu et al. (2017)).

Weigel et al. (2021a) showed that the freshly nucleated aerosol particles (as observed from COPAS) coagulate onto the background aerosol (as observed by the UHSAS-A) within a few hours by using simple box model simulations (adopting the SOCOL (SOlar Climate Ozone Links (Stenke et al. (2013)) coagulation subroutines). Because of the short periods of time available to detect recent NPF events and the still frequent NPF encounters during StratoClim 2017 detected by COPAS indicate the prevalence of such events within the ASM region (Weigel et al. (2021a); Weigel et al. (2021b)). Still these simulations suggests that the coagulation of freshly nucleated aerosol particles alone cannot cause the lower part of the aerosol size distribution as measured by the UHSAS-A inside the ATALs altitude range. Also the question remains open, where the particles larger than roughly 500 to 800 nm in the UHSAS-A size distributions come from. Condensational growth could be a major process, although the nature and amounts of the various possible condensable gases are not yet well known. Furthermore, the upward transport of already existing larger aerosol particles (Yuan et al. (2019)) can contribute to the overall size distributions as observed by the UHSAS-A. Because of this complex interaction between dynamical and microphysical processes further, much more advanced model simulations are needed to identify and quantify the importance of various involved processes. To support such model simulations our data are well suited, because the UHSAS-A particle size distributions extend down to 65 nm while COPAS measured simultaneously with three different lower detection limits from 6 nm up to 15 nm.

Data availability. The data shown in this study will be available from the HALO database at https://halo-db.pa.op.dlr.de/mission/101 (last access: 30 August 2021) (German Aerospace Center (2021)), or they may be provided by respective PI upon request.

Appendix A: UHSAS-A characterization

A1 Pump test and sample flow calibration

The UHSAS-A discussed in this study performed its first in-flight measurements aboard the research aircraft M 55 Geophysica during the StratoClim 2016 field campaign in Kalamata (Greece). This measurement flights as well as tests in a low pressure chamber have shown, that the UHSAS-A sample flow, purge flow, sheath flow, and also the ratio between sheath flow and sample flow are not stable at pressure levels lower than ~ 120 hPa (see Fig. A1 (a)), when using the standard pump system. For this reason a new pump system was integrated into the UHSAS-A. The new set-up was tested and characterized in an in-house built low pressure chamber at pressure levels as low as ~ 45 hPa. Figure A1 (b) and (c) show that all internal flows of the UHSAS-A were stable during the low pressure chamber test and during the StratoClim 2017 mission flights (flight KTM 4 shown as example case with some of the lowest pressure levels reached during the campaign) for pressure levels as low as 45 or 55 hPa, respectively. The minor but visible variability of the ratio between the sample and the sheath flow (Fig. A1 (c)), within the region on the cold point tropopause, could only be related to a high frequency variability (up to ± 1 degree) of the aircraft's angle of attack. This variability is not expected to have a significant influence on the UHSAS-A measurement performance.

Figure A2 shows the results of the sample flow characterization measurements as a function of pressure. For these measurements the UHSAS-A was located in the low pressure chamber and directly connected through a chamber outlet via a high precision needle valve with a reference flow-meter (Gilibrator, Version 2, manufacturer: SENSIDYNE) located outside of the chamber. For each calibration point the needle valve was closed a little more. After the sample flow (regulated to 50 cm^3 min^{-1}) of the UHSAS-A (Q_{UHSAS}) and the pressure measured at the UHSAS-A optical measurement cell were stable, the flow measurements with the Gilibrator were done for the respective calibration point. The results of these reference measurements were converted to the pressure conditions measured by the UHSAS-A inside the low pressure chamber ($Q_{Gilibrator}$), making the idealized assumption that the temperature of the air inside the UHSAS-A flow system was equal to the temperature in the laboratory. The ratio $F_Q = Q_{Gilibrator}/Q_{UHSAS}$ as a function of the pressure measured in the UHSAS-A optical measurement cell is shown in Fig. A2. The vertical bars represent the results of the error propagation calculated on the basis of the individual uncertainties of the measurements from the flow- and pressure-meters.

$$Q_{UHSAS\_cali} = Q_{UHSAS} \cdot \left[y_0 + A \exp \left\{ -\left(\frac{\ln\left(\frac{p_{UHSAS}}{x_0}\right)}{width} \right)^2 \right\} \right] \tag{A1}$$

The calculated log-normal fit function (coefficients reported in Fig. A2) together with Eq. A1 allow for a calibration of the sample flow measurement (Q_{UHSAS}) as a function of pressure (p_{UHSAS}) to Q_{UHSAS_cali}.

A2 Particle sizing

Since the UHSAS-A measures the particle size based on the intensity of the laser light scattered by the individual aerosol particles, the particle size determination is also dependent on the species of the aerosol particle. As described in Sec. 3.1, the calibration of the UHSAS-A was performed with PSL particle standards that were additional size-selected by a DMA (TSI

3080 with TSI 3081), while we want to measure complex mixtures of different aerosol particle species in the free atmosphere. In order to confirm the previous size calibration with PSL particle standards, first measurements with PSL particles of different sizes were carried out. Subsequently, as already shown by Cai et al. (2008) for the laboratory version of the UHSAS, measurements with sodium chloride, ammonium nitrate, and ammonium sulfate were carried out.

For each particle size and species, size distributions averaged over several minutes were generated. The DMA allowed the selection of particles with diameters up to 1 µm. Therefore, measurements at the upper end of the UHSAS-A sizing range could be performed. For particle diameters larger than 600 nm, however, only with high concentrations of preselected PSL standards a sufficient number of particles could be provided to the UHSAS-A, to allow for the measurement with low variability due to counting statistics. For sodium chloride, ammonium nitrate, and ammonium sulfate, the aerosol generator used was not able to generate enough particles of these sizes. Hence, after the selection by the DMA and possible line losses, only an insufficient number of these large particles could reach the detection cell of the UHSAS-A. Figure A3 shows the results of these measurements, comparing the main particle mode diameter of the size distribution measured by the UHSAS-A (using all 99 available size bins) compared to the particle' (electrical mobility) diameter selected by a DMA for different particle species. The gray bars represent the bin mapping used after the post processing. These bin-limits were selected as a compromise between the size resolution and a reasonable averaging time at low number concentrations, as well as the ability of the UHSAS-A to resolve the signal response (most relevant for particles with diameter > 600 nm).

For each particle species a linear regressions was calculated. Considering the slopes of the linear regression function for PSL particles with a value of 0.99, there is a discrepancy of only 1 % between the DMA set mobility diameter and the measurement from the UHSAS-A. Comparing the slopes of the linear regressions of sodium chloride, ammonium nitrate, and ammonium sulfate with those reported by Cai et al. (2008), for results obtained with the laboratory version of the UHSAS, the particle size measurements of both instruments show a similar dependence on the particle species. For example, the slopes of sodium chloride at 0.96 ± 0.01 and ammonium nitrate at 0.92 ± 0.01 in Cai et al. (2008) agree, within the confidence interval, with the slopes determined here of 0.97 ± 0.01 for sodium chloride and 0.91 ± 0.01 for ammonium nitrate. However, ammonium sulfate, with a slope of 0.89 ± 0.01 for the UHSAS-A, shows a much larger deviation from the DMA diameter than that reported by Cai et al. (2008) with 0.96 ± 0.01. This could, for example, be due to insufficient drying of the particles in the diffusion dryer. In order to exclude this, Cai et al. (2008) also measured the relative humidity in their system and reported it as RH < 15 %. Since the relative humidity was not measured in the experimental setup used here, an influence of residual moisture on the measurement cannot be excluded.

Based on limited laboratory studies, Kupc et al. (2018) reported that black carbon particles might incandesce and vaporize due to the particles' absorption of energy of the UHSAS-A detector laser (optical cavity laser power: $\sim 1 \text{ kW cm}^{-2}$ at 1054 nm). This effect and the complex refractive index of black carbon would alter the sizing of black carbon particles significantly. While particles might be undersized because of the complex refractive index, the incandescing of black carbon particles could potentially result in an oversizing or an undersizing of these particles.

A3 Counting efficiency

To characterize the counting efficiency of the UHSAS-A, the aerosol-line between the DMA and the UHSAS-A (as described in Appendix A2) was split and one line was connected to a condensation particle counter (CPC, TSI 3025A) as reference. In total 32 measuring series with PSL, sodium chloride, ammonium nitrate, and ammonium sulfate particles in different sizes (selected with a DMA) and number concentrations (between 30 and 2000 cm^{-3}), each averaged over 100 seconds, were conducted. The results of these measurements are shown in Fig. A4, with the electrical mobility diameter set at the DMA color-coded. The correlation coefficient $R^2 = 0.97$ confirms the linear correlation between the particle number concentrations measured by the UHSAS-A and the CPC over three orders of magnitude. The slope of the linear fit function was calculated to be 1.06, while the intercept was forced to be 0 (after successful zero filter tests with both instruments). A dependence on the particle size is not visible in the here used particle size range. Therefore, the accuracy of the particle number concentration measured by the UHSAS-A under laboratory conditions was estimated to be 10 %, limited by the accuracy reported for the reference instrument (CPC).

A4 Recalibration of the UHSAS-A bin-limits

The UHSAS-A was calibrated with PSL standard particles as described in Sec. 3.1. These particles have a refractive index of m = 1.59 (Heim et al. (2008)). For the aerosol backscatter calculations (Sec. 6.1) the bin-limits were recalibrated for a refractive index of m = 1.45 and m = 1.5 (see Table A1). This was done by calculating the response of the UHSAS-A (laser wavelength: 1054 nm; collection angle: 22° to 158° as reported by Cai et al. (2008)) using an in-house written software by Vetter (2004), which is based on the algorithms described in Bohren and Huffmann (2008). Figure A5 shows the relative intensity at the detector, calculated for these three refractive indices.

Appendix B: Sensitivity of the backscatter calculation to particle size and refractive index

To estimate the influence of the uncertainties from the aerosol particle size distribution measurements on the aerosol backscatter calculations, a sensitivity study was performed as follows: The aerosol backscatter coefficient was calculated for a set of 42 size distributions (each averaged over a 100 second interval) from StratoClim 2017 flight KTM3 using a refractive index of m = 1.5. Then the calculations were repeated after the bin-limits of the size distributions were shifted by 10 % to larger values and once more after the values of the bin-limits were made 10 % smaller than the reference case. As a next step the backscatter calculations were done using the original bin-limits changing the refractive index to 1.45 and once more to 1.55. The results of these calculations (Fig. A6) do not vary by more than 50 % from the reference case. This also agrees with the variations of the backscatter calculations reported in Cairo et al. (2011).

Table A1. UHSAS-A bin-limits for the calibration with PSL particles (refractive index m =1.59), recalibrated for refractive indices of 1.5 and 1.45.

bin-limits in nm for m = 1.59	bin-limits in nm for m = 1.5	bin-limits in nm for m = 1.45
65	68	70
71	74	76
79	82	85
88	92	95
104	109	112
123	128	133
145	152	157
171	179	185
213	224	232
266	280	290
341	361	376
449	481	503
592	641	674
1000	1061	1111

635 **Appendix C: BR variability of the remote sensing measurements during StratoClim 2017**

The standard deviation for the backscatter ratio profile calculated based on the aerosol particle size distributions measured during StratoClim 2017 was already shown in Fig. 7. Figure A7 additionally reports the standard deviation for the backscatter ratio profiles measured by CALIOP, MAS, and MAL as horizontal bars.

Author contributions. CM performed the UHSAS-A measurements and data evaluations, created the figures and drafted the manuscript with
640 contributions by SB, RW, FC, and JPV. RW provided the COPAS aerosol measurements. FC provided the MAS backscatter ratio profile and performed the backscatter ratio calculations based on the prepared aerosol size distributions by CM. JPV provided the CALIOP backscatter ratio profile. VM and RM provided the MAL backscatter ratio profile. The NIXE-CAS data was provided by AA and MK. FP contributed with meteorological re-analyses. SV and FD'A provided the CO data. TD provided the balloon-borne aerosol size distribution measurement data. The manuscript was critically reviewed by RW, FC, JPV, AA, MK, VM, RM, SV, FD'A, FP, TD, and SB.

645 *Competing interests.* The authors declare that they have no conflict of interest.

Acknowledgements. The contributions from the technical staff at the workshops of the MPI for Chemistry and the Institute for Physics of the Atmosphere (Mainz University), as well as the Myasishchev Design Bureau (MDB) were essential. In particular, we acknowledge support of T. Böttger, C. von Glahn, H. Rott, and W. Schneider. The extraordinary commitment of F. Stroh in realisation of the campaign and the leadership of the entire StratoClim project by M. Rex are gratefully acknowledged. We very much thank the MDB crew and the M55 Geophysica pilots. Some of our research leading to the presented results received funding from the European Research Council under the European Union's Seventh Framework Program (FP/2007-2013)/ERC Grant Agreement No. 321040 (EXCATRO). The StratoClim project was funded by the EU (FP7/2007–2018 Grant No. 603557) and also supported by the German "Bundesministerium für Bildung und Forschung" (BMBF) under the joint ROMIC-project SPITFIRE (01LG1205A). The balloon-borne LPC & CNC measurements from Hyderabad were supported by the US National Aeronautics and Space Administration, and from Laramie by the US National Science Foundation, award #1011827. We explicitly thank the Nepalese government authorities, research institutions, and Tribhuvan Airport, as well as the German Embassy for their extraordinary support and hospitality, since without them this exceptional field campaign and our research would not have been possible.

References

Baumgardner, D., Abel, S. J., Axisa, D., Cotton, R., Crosier, J., Field, P., Gurganus, C., Heymsfield, A., Korolev, A., Krämer, M., Lawson, P., McFarquhar, G., Ulanowski, Z., and Um, J.: Cloud ice properties: In situ measurement challenges, Meteor. Mon., 58, 91–923, https://doi.org/10.1175/amsmonographs-d-16-0011.1, 2017.

Baumgartner, M., Weigel, R., Harvey, A. H., Ploeger, F., Achatz, U., and Spichtinger, P.: Reappraising the appropriate calculation of a common meteorological quantity: potential temperature, Atmos. Chem. Phys., 20, 15 585–15 616, https://doi.org/10.5194/acp-20-15585-2020, 2020.

Bohren, C. F. and Huffmann, D. R.: Absorption and scattering of light by small particles, Wiley and Sons, 2008.

Borrmann, S., Stefanutti, L., and Khattatov, V.: Chemistry and aerosol measurements on the Geophysika stratospheric research aircraft: The airborne polar experiment, Phys. Chem. Earth., 20, 97–101, https://doi.org/10.1016/0079-1946(95)00011-X, 1995.

Borrmann, S., Kunkel, D., Weigel, R., Minikin, A., Deshler, T., Wilson, J. C., Curtius, J., Volk, C. M., Homan, C. D., Ulanovsky, A., Ravegnani, F., Viciani, S., Shur, G. N., Belyaev, G. V., Law, K. S., and Cairo, F.: Aerosols in the tropical and subtropical UT/LS: in-situ measurements of submicron particle abundance and volatility, Atmos. Chem. Phys., 10, 5573–5592, https://doi.org/10.5194/acp-10-5573-2010, 2010.

Brock, C. A., Hamill, P., Wilson, J. C., Jonsson, H. H., and Chan, K. R.: Particle formation in the upper tropical troposphere: A source of nuclei for the stratospheric aerosol, Science, 270, 1650–1653, https://doi.org/10.1126/science.270.5242.1650, 1995.

Brunamonti, S., Jorge, T., Oelsner, P., Hanumanthu, S., Singh, B. B., Kumar, K. R., Sonbawne, S., Meier, S., Singh, D., Wienhold, F. G., Luo, B. P., Boettcher, M., Poltera, Y., Jauhiainen, H., Kayastha, R., Karmacharya, J., Dirksen, R., Naja, M., Rex, M., Fadnavis, S., and Peter, T.: Balloon-borne measurements of temperature, water vapor, ozone and aerosol backscatter on the southern slopes of the Himalayas during StratoClim 2016–2017, Atmos. Chem. Phys., 18, 15 937–15 957, https://doi.org/10.5194/acp-18-15937-2018, 2018.

Bucci, S., Legras, B., Sellitto, P., D'Amato, F., Viciani, S., Montori, A., Chiarugi, A., Ravegnani, F., Ulanovsky, A., Cairo, F., and Stroh, F.: Deep-convective influence on the upper troposphere–lower stratosphere composition in the Asian monsoon anticyclone region: 2017 StratoClim campaign results, Atmos. Chem. Phys., 20, 12 193–12 210, https://doi.org/10.5194/acp-20-12193-2020, 2020.

Cai, Y., Montague, D. C., Mooiweer-Bryan, W., and Deshler, T.: Performance characteristics of the ultra high sensitivity aerosol spectrometer for particles between 55 and 800 nm: Laboratory and field studies, J. Aerosol Sci., 39, 759 – 769, https://doi.org/10.1016/j.jaerosci.2008.04.007, 2008.

Cairo, F.: Polar stratospheric clouds observed during the Airborne Polar Experiment–Geophysica Aircraft in Antarctica (APE-GAIA) campaign, J. Geophys. Res., 109, https://doi.org/10.1029/2003jd003930, 2004.

Cairo, F., Di Donfrancesco, G., Snels, M., Fierli, F., Viterbini, M., Borrmann, S., and Frey, W.: A comparison of light backscattering and particle size distribution measurements in tropical cirrus clouds, Atmos. Meas. Tech., 4, 557–570, https://doi.org/10.5194/amt-4-557-2011, 2011.

Campbell, P. and Deshler, T.: Condensation nuclei measurements in the midlatitude (1982-2012) and Antarctic (1986-2010) stratosphere between 20 and 35 km, J. Geophys. Res.-Atmos., 119, 137–152, https://doi.org/10.1002/2013jd019710, 2014.

Collis, R. T. H. and Russell, P. B.: Lidar measurement of particles and gases by elastic backscattering and differential absorption, in: Laser monitoring of the atmosphere, edited by: Hinkley, E.D., Springer Verlag, Berlin, Germany, https://doi.org/10.1007/3-540-07743-x, 1976.

Costa, A., Meyer, J., Afchine, A., Luebke, A., Günther, G., Dorsey, J. R., Gallagher, M. W., Ehrlich, A., Wendisch, M., Baumgardner, D., Wex, H., and Krämer, M.: Classification of Arctic, midlatitude and tropical clouds in the mixed-phase temperature regime, Atmos. Chem. Phys., 17, 12 219–12 238, https://doi.org/10.5194/acp-17-12219-2017, 2017.

695 Croft, B., Lohmann, U., Martin, R. V., Stier, P., Wurzler, S., Feichter, J., Hoose, C., Heikkilä, U., van Donkelaar, A., and Ferrachat, S.: Influences of in-cloud aerosol scavenging parameterizations on aerosol concentrations and wet deposition in ECHAM5-HAM, Atmos. Chem. Phys., 10, 1511–1543, https://doi.org/10.5194/acp-10-1511-2010, 2010.

Curtius, J., Weigel, R., Vössing, H.-J., Wernli, H., Werner, A., Volk, C.-M., Konopka, P., Krebsbach, M., Schiller, C., Roiger, A., Schlager, H., Dreiling, V., and Borrmann, S.: Observations of meteoric material and implications for aerosol nucleation in the winter Arctic lower

700 stratosphere derived from in situ particle measurements, Atmos. Chem. Phys., 5, 3053–3069, https://doi.org/10.5194/acp-5-3053-2005, 2005.

Deshler, T., Hervig, M. E., Hofmann, D. J., Rosen, J. M., and Liley, J. B.: Thirty years of in situ stratospheric aerosol size distribution measurements from Laramie, Wyoming (41°N), using balloon-borne instruments, J. Geophys. Res.-Atmos., 108, https://doi.org/10.1029/2002JD002514, 2003.

705 Deshler, T., Luo, B., Kovilakam, M., Peter, T., and Kalnajs, L. E.: Retrieval of aerosol size distributions from in situ particle counter measurements: Instrument counting efficiency and comparisons with satellite measurements, J. Geophys. Res.-Atmos., 124, 5058–5087, https://doi.org/10.1029/2018jd029558, 2019.

Dunkerton, T. J.: Evidence of meridional motion in the summer lower stratosphere adjacent to monsoon regions, J. Geophys. Res.-Atmos., 100, 16 675–16 688, https://doi.org/10.1029/95JD01263, 1995.

710 Fairlie, T. D., Liu, H., Vernier, J.-P., Campuzano-Jost, P., Jimenez, J. L., Jo, D. S., Zhang, B., Natarajan, M., Avery, M. A., and Huey, G.: Estimates of regional source contributions to the Asian tropopause aerosol layer using a chemical transport model, J. Geophys. Res.-Atmos., 125, https://doi.org/10.1029/2019jd031506, 2020.

Fierli, F., Orlandi, E., Law, K. S., Cagnazzo, C., Cairo, F., Schiller, C., Borrmann, S., Donfrancesco, G. D., Ravegnani, F., and Volk, C. M.: Impact of deep convection in the tropical tropopause layer in West Africa: in-situ observations and mesoscale modelling, Atmos. Chem.

715 Phys., 11, 201–214, https://doi.org/10.5194/acp-11-201-2011, 2011.

Fueglistaler, S., Dessler, A. E., Dunkerton, T. J., Folkins, I., Fu, Q., and Mote, P. W.: Tropical tropopause layer, Rev. Geophys., 47, https://doi.org/10.1029/2008RG000267, 2009.

Garny, H. and Randel, W. J.: Transport pathways from the Asian monsoon anticyclone to the stratosphere, Atmos. Chem. Phys., 16, 2703–2718, https://doi.org/10.5194/acp-16-2703-2016, 2016.

720 German Aerospace Center: HALO database, available at: https://halo-db.pa.op.dlr.de/mission/101, last access: 30 August, 2021.

Gu, Y., Liao, H., and Bian, J.: Summertime nitrate aerosol in the upper troposphere and lower stratosphere over the Tibetan Plateau and the South Asian summer monsoon region, Atmos. Chem. Phys., 16, 6641–6663, https://doi.org/10.5194/acp-16-6641-2016, 2016.

Hanumanthu, S., Vogel, B., Müller, R., Brunamonti, S., Fadnavis, S., Li, D., Ölsner, P., Naja, M., Singh, B. B., Kumar, K. R., Sonbawne, S., Jauhiainen, H., Vömel, H., Luo, B., Jorge, T., Wienhold, F. G., Dirkson, R., and Peter, T.: Strong day-to-day variability

725 of the Asian tropopause aerosol layer (ATAL) in August 2016 at the Himalayan foothills, Atmos. Chem. Phys., 20, 14 273–14 302, https://doi.org/10.5194/acp-20-14273-2020, 2020.

Heim, M., Mullins, B. J., Umhauer, H., and Kasper, G.: Performance evaluation of three optical particle counters with an efficient "multimodal" calibration method, J. Aerosol Sci., 39, 1019–1031, https://doi.org/10.1016/j.jaerosci.2008.07.006, 2008.

Höpfner, M., Ungermann, J., Borrmann, S., Wagner, R., Spang, R., Riese, M., Stiller, G., Appel, O., Batenburg, A. M., Bucci, S., Cairo, F., Dragoneas, A., Friedl-Vallon, F., Hünig, A., Johansson, S., Krasauskas, L., Legras, B., Leisner, T., Mahnke, C., Möhler, O., Molleker, S., Müller, R., Neubert, T., Orphal, J., Preusse, P., Rex, M., Saathoff, H., Stroh, F., Weigel, R., and Wohltmann, I.: Ammonium nitrate particles formed in upper troposphere from ground ammonia sources during Asian monsoons, Nat. Geosci., 12, 608–612, https://doi.org/10.1038/s41561-019-0385-8, 2019.

Junge, C. E., Chagnon, C. W., and Manson, J. E.: A world-wide stratospheric aerosol layer, Science, 133, 1478–1479, https://doi.org/10.1126/science.133.3463.1478-a, 1961.

Kremser, S., Thomason, L. W., von Hobe, M., Hermann, M., Deshler, T., Timmreck, C., Toohey, M., Stenke, A., Schwarz, J. P., Weigel, R., Fueglistaler, S., Prata, F. J., Vernier, J.-P., Schlager, H., Barnes, J. E., Antuña-Marrero, J.-C., Fairlie, D., Palm, M., Mahieu, E., Notholt, J., Rex, M., Bingen, C., Vanhellemont, F., Bourassa, A., Plane, J. M. C., Klocke, D., Carn, S. A., Clarisse, L., Trickl, T., Neely, R., James, A. D., Rieger, L., Wilson, J. C., and Meland, B.: Stratospheric aerosol—Observations, processes, and impact on climate, Rev. Geophys., 54, 278–335, https://doi.org/10.1002/2015RG000511, 2016.

Kupc, A., Williamson, C., Wagner, N. L., Richardson, M., and Brock, C. A.: Modification, calibration, and performance of the Ultra-High Sensitivity Aerosol Spectrometer for particle size distribution and volatility measurements during the Atmospheric Tomography Mission (ATom) airborne campaign, Atmos. Meas. Tech., 11, 369–383, https://doi.org/10.5194/amt-11-369-2018, 2018.

Mitev, V., Poole, L. R., Pitts, M. C., and Matthey, R.: Comparison case between CALIPSO lidar and MALs on M55 Geophysica during RECONCILE campaign, in: 26th International Laser Radar Conference, 25-29 June 2012, Porto Heli Greece, Proceedings Vol. II, 729-732, 2012.

Mitev, V., Matthey, R., and Makarov, V.: Backscatter-depolarisation lidars on high-altitude research aircraft, in: 20th International Symposium on Atmospheric and Ocean Optics: Atmospheric Physics, edited by Romanovskii, O. A., SPIE, https://doi.org/10.1117/12.2075634, 2014.

Molleker, S., Borrmann, S., Schlager, H., Luo, B., Frey, W., Klingebiel, M., Weigel, R., Ebert, M., Mitev, V., Matthey, R., Woiwode, W., Oelhaf, H., Dörnbrack, A., Stratmann, G., Grooß, J.-U., Günther, G., Vogel, B., Müller, R., Krämer, M., Meyer, J., and Cairo, F.: Microphysical properties of synoptic-scale polar stratospheric clouds: in situ measurements of unexpectedly large HNO_3-containing particles in the Arctic vortex, Atmos. Chem. Phys., 14, 10 785–10 801, https://doi.org/10.5194/acp-14-10785-2014, 2014.

Neely, R. R., Yu, P., Rosenlof, K. H., Toon, O. B., Daniel, J. S., Solomon, S., and Miller, H. L.: The contribution of anthropogenic SO2 emissions to the Asian tropopause aerosol layer, J. Geophys. Res.-Atmos., 119, 1571–1579, https://doi.org/10.1002/2013JD020578, 2014.

Pan, L. L., Honomichl, S. B., Kinnison, D. E., Abalos, M., Randel, W. J., Bergman, J. W., and Bian, J.: Transport of chemical tracers from the boundary layer to stratosphere associated with the dynamics of the Asian summer monsoon, J. Geophys. Res.-Atmos., 121, 14,159–14,174, https://doi.org/10.1002/2016jd025616, 2016.

Park, M., Randel, W. J., Gettelman, A., Massie, S. T., and Jiang, J. H.: Transport above the Asian summer monsoon anticyclone inferred from aura microwave limb sounder tracers, J. Geophys. Res.-Atmos., 112, https://doi.org/10.1029/2006JD008294, 2007.

Park, M., Randel, W. J., Emmons, L. K., and Livesey, N. J.: Transport pathways of carbon monoxide in the Asian summer monsoon diagnosed from model of ozone and related tracers (MOZART), J. Geophys. Res., 114, https://doi.org/10.1029/2008jd010621, 2009.

Ploeger, F., Gottschling, C., Griessbach, S., Grooß, J.-U., Guenther, G., Konopka, P., Müller, R., Riese, M., Stroh, F., Tao, M., Ungermann, J., Vogel, B., and von Hobe, M.: A potential vorticity-based determination of the transport barrier in the Asian summer monsoon anticyclone, Atmos. Chem. Phys., 15, 13 145–13 159, https://doi.org/10.5194/acp-15-13145-2015, 2015.

Prata, A. J., Carn, S. A., Stohl, A., and Kerkmann, J.: Long range transport and fate of a stratospheric volcanic cloud from Soufrière Hills volcano, Montserrat, Atmos. Chem. Phys., 7, 5093–5103, https://doi.org/10.5194/acp-7-5093-2007, 2007.

Randel, W. J. and Jensen, E. J.: Physical processes in the tropical tropopause layer and their roles in a changing climate, Nat. Geosci., 6, 169, https://doi.org/10.1038/ngeo1733, 2013.

Randel, W. J. and Park, M.: Deep convective influence on the Asian summer monsoon anticyclone and associated tracer variability observed with Atmospheric Infrared Sounder (AIRS), J. Geophys. Res., 111, https://doi.org/10.1029/2005jd006490, 2006.

Sokolov, L. and Lepuchov, B.: Protocol of interaction between Unit for Connection with Scientific Equipment (UCSE) and on-board scientific equipment of Geophysica aircraft (Second edition), 1998.

Stefanutti, L., Sokolov, L., Balestri, S., MacKenzie, A. R., and Khattatov, V.: The M-55 Geophysica as a platform for the Airborne Polar Experiment, J. Atmos. Ocean. Tech., 16, 1303 – 1312, https://doi.org/10.1175/1520-0426(1999)016<1303:TMGAAP>2.0.CO;2, 1999.

Stenke, A., Schraner, M., Rozanov, E., Egorova, T., Luo, B., and Peter, T.: The SOCOL version 3.0 chemistry–climate model: description, evaluation, and implications from an advanced transport algorithm, Geosci. Model. Dev., 6, 1407–1427, https://doi.org/10.5194/gmd-6-1407-2013, 2013.

Vernier, J. P., Pommereau, J. P., Garnier, A., Pelon, J., Larsen, N., Nielsen, J., Christensen, T., Cairo, F., Thomason, L. W., Leblanc, T., and McDermid, I. S.: Tropical stratospheric aerosol layer from CALIPSO lidar observations, J. Geophys. Res., 114, https://doi.org/10.1029/2009jd011946, 2009.

Vernier, J.-P., Thomason, L. W., and Kar, J.: CALIPSO detection of an Asian tropopause aerosol layer, Geophys. Res. Lett., 38, https://doi.org/10.1029/2010GL046614, 2011.

Vernier, J.-P., Fairlie, T. D., Natarajan, M., Wienhold, F. G., Bian, J., Martinsson, B. G., Crumeyrolle, S., Thomason, L. W., and Bedka, K. M.: Increase in upper tropospheric and lower stratospheric aerosol levels and its potential connection with Asian pollution, J. Geophys. Res.-Atmos., 120, 1608–1619, https://doi.org/10.1002/2014jd022372, 2015.

Vernier, J.-P., Fairlie, T. D., Deshler, T., Ratnam, M. V., Gadhavi, H., Kumar, B. S., Natarajan, M., Pandit, A. K., Raj, S. T. A., Kumar, A. H., Jayaraman, A., Singh, A. K., Rastogi, N., Sinha, P. R., Kumar, S., Tiwari, S., Wegner, T., Baker, N., Vignelles, D., Stenchikov, G., Shevchenko, I., Smith, J., Bedka, K., Kesarkar, A., Singh, V., Bhate, J., Ravikiran, V., Rao, M. D., Ravindrababu, S., Patel, A., Vernier, H., Wienhold, F. G., Liu, H., Knepp, T. N., Thomason, L., Crawford, J., Ziemba, L., Moore, J., Crumeyrolle, S., Williamson, M., Berthet, G., Jégou, F., and Renard, J.-B.: BATAL: The balloon measurement campaigns of the Asian tropopause aerosol layer, B. Am. Meteorol. Soc., 99, 955–973, https://doi.org/10.1175/bams-d-17-0014.1, 2018.

Vetter, T.: Berechnung der Mie-Streufunktionen zur Kalibrierung optischer Partikelzähler, Diploma thesis (in German), University Mainz, 2004.

Viciani, S., D'Amato, F., Mazzinghi, P., Castagnoli, F., Toci, G., and Werle, P.: A cryogenically operated laser diode spectrometer for airborne measurement of stratospheric trace gases, Appl. Phys. B-Lasers. O., 90, 581–592, https://doi.org/10.1007/s00340-007-2885-2, 2008.

Viciani, S., Montori, A., Chiarugi, A., and D'Amato, F.: A portable quantum cascade laser spectrometer for atmospheric measurements of carbon monoxide, Sensors, 18, 2380, https://doi.org/10.3390/s18072380, 2018.

Vogel, B., Günther, G., Müller, R., Grooß, J.-U., and Riese, M.: Impact of different Asian source regions on the composition of the Asian monsoon anticyclone and of the extratropical lowermost stratosphere, Atmos. Chem. Phys., 15, 13 699–13 716, https://doi.org/10.5194/acp-15-13699-2015, 2015.

Vogel, B., Müller, R., Günther, G., Spang, R., Hanumanthu, S., Li, D., Riese, M., and Stiller, G. P.: Lagrangian simulations of the transport of young air masses to the top of the Asian monsoon anticyclone and into the tropical pipe, Atmos. Chem. Phys., 19, 6007–6034, https://doi.org/10.5194/acp-19-6007-2019, 2019.

von Hobe, M., Ploeger, F., Konopka, P., Kloss, C., Ulanowski, A., Yushkov, V., Ravegnani, F., Volk, C. M., Pan, L. L., Honomichl, S. B., Tilmes, S., Kinnison, D. E., Garcia, R. R., and Wright, J. S.: Upward transport into and within the Asian monsoon anticyclone as inferred from StratoClim trace gas observations, Atmos. Chem. Phys., 21, 1267–1285, https://doi.org/10.5194/acp-21-1267-2021, 2021.

Wagner, R., Bertozzi, B., Höpfner, M., Höhler, K., Möhler, O., Saathoff, H., and Leisner, T.: Solid ammonium nitrate aerosols as efficient ice nucleating particles at cirrus temperatures, J. Geophys. Res.-Atmos., 125, https://doi.org/10.1029/2019jd032248, 2020.

Wang, M., Kong, W., Marten, R., He, X.-C., Chen, D., Pfeifer, J., Heitto, A., Kontkanen, J., Dada, L., Kürten, A., Yli-Juuti, T., Manninen, H. E., Amanatidis, S., Amorim, A., Baalbaki, R., Baccarini, A., Bell, D. M., Bertozzi, B., Bräkling, S., Brilke, S., Murillo, L. C., Chiu, R., Chu, B., Menezes, L.-P. D., Duplissy, J., Finkenzeller, H., Carracedo, L. G., Granzin, M., Guida, R., Hansel, A., Hofbauer, V., Krechmer, J., Lehtipalo, K., Lamkaddam, H., Lampimäki, M., Lee, C. P., Makhmutov, V., Marie, G., Mathot, S., Mauldin, R. L., Mentler, B., Müller, T., Onnela, A., Partoll, E., Petäjä, T., Philippov, M., Pospisilova, V., Ranjithkumar, A., Rissanen, M., Rörup, B., Scholz, W., Shen, J., Simon, M., Sipilä, M., Steiner, G., Stolzenburg, D., Tham, Y. J., Tomé, A., Wagner, A. C., Wang, D. S., Wang, Y., Weber, S. K., Winkler, P. M., Wlasits, P. J., Wu, Y., Xiao, M., Ye, Q., Zauner-Wieczorek, M., Zhou, X., Volkamer, R., Riipinen, I., Dommen, J., Curtius, J., Baltensperger, U., Kulmala, M., Worsnop, D. R., Kirkby, J., Seinfeld, J. H., El-Haddad, I., Flagan, R. C., and Donahue, N. M.: Rapid growth of new atmospheric particles by nitric acid and ammonia condensation, Nature, 581, 184–189, https://doi.org/10.1038/s41586-020-2270-4, 2020.

Ward, S. M., Deshler, T., and Hertzog, A.: Quasi-Lagrangian measurements of nitric acid trihydrate formation over Antarctica, J. Geophys. Res.-Atmos., 119, 245–258, https://doi.org/10.1002/2013JD020326, 2014.

Weigel, R., Hermann, M., Curtius, J., Voigt, C., Walter, S., Böttger, T., Lepukhov, B., Belyaev, G., and Borrmann, S.: Experimental characterization of the COndensation PArticle counting System for high altitude aircraft-borne application, Atmos. Meas. Tech., 2, 243–258, https://doi.org/10.5194/amt-2-243-2009, 2009.

Weigel, R., Borrmann, S., Kazil, J., Minikin, A., Stohl, A., Wilson, J. C., Reeves, J. M., Kunkel, D., de Reus, M., Frey, W., Lovejoy, E. R., Volk, C. M., Viciani, S., D'Amato, F., Schiller, C., Peter, T., Schlager, H., Cairo, F., Law, K. S., Shur, G. N., Belyaev, G. V., and Curtius, J.: In situ observations of new particle formation in the tropical upper troposphere: the role of clouds and the nucleation mechanism, Atmos. Chem. Phys., 11, 9983–10 010, https://doi.org/10.5194/acp-11-9983-2011, 2011.

Weigel, R., Volk, C. M., Kandler, K., Hösen, E., Günther, G., Vogel, B., Grooß, J.-U., Khaykin, S., Belyaev, G. V., and Borrmann, S.: Enhancements of the refractory submicron aerosol fraction in the Arctic polar vortex: feature or exception?, Atmos. Chem. Phys., 14, 12 319–12 342, https://doi.org/10.5194/acp-14-12319-2014, 2014.

Weigel, R., Mahnke, C., Baumgartner, M., Dragoneas, A., Vogel, B., Ploeger, F., Viciani, S., D'Amato, F., Bucci, S., Legras, B., Luo, B., and Borrmann, S.: In situ observation of new particle formation (NPF) in the tropical tropopause layer of the 2017 Asian monsoon anticyclone – Part 1: Summary of StratoClim results, Atmos. Chem. Phys., 21, 11 689–11 722, https://doi.org/10.5194/acp-21-11689-2021, 2021a.

Weigel, R., Mahnke, C., Baumgartner, M., Krämer, M., Spichtinger, P., Spelten, N., Afchine, A., Rolf, C., Viciani, S., D'Amato, F., Tost, H., and Borrmann, S.: In situ observation of new particle formation (NPF) in the tropical tropopause layer of the 2017 Asian monsoon anticyclone – Part 2: NPF inside ice clouds, Atmos. Chem. Phys., 21, 13 455–13 481, https://doi.org/10.5194/acp-21-13455-2021, 2021b.

Williamson, C. J., Kupc, A., Axisa, D., Bilsback, K. R., Bui, T., Campuzano-Jost, P., Dollner, M., Froyd, K. D., Hodshire, A. L., Jimenez, J. L., Kodros, J. K., Luo, G., Murphy, D. M., Nault, B. A., Ray, E. A., Weinzierl, B., Wilson, J. C., Yu, F., Yu, P., Pierce, J. R., and Brock, C. A.: A large source of cloud condensation nuclei from new particle formation in the tropics, Nature, 574, 399–403, https://doi.org/10.1038/s41586-019-1638-9, 2019.

Winker, D. M., Pelon, J., Coakley, J. A., Ackerman, S. A., Charlson, R. J., Colarco, P. R., Flamant, P., Fu, Q., Hoff, R. M., Kittaka, C., Kubar, T. L., Treut, H. L., Mccormick, M. P., Mégie, G., Poole, L., Powell, K., Trepte, C., Vaughan, M. A., and Wielicki, B. A.: The CALIPSO mission, B. Am. Meteorol. Soc., 91, 1211–1230, https://doi.org/10.1175/2010bams3009.1, 2010.

WMO: International Meteorological Tables, WMO-No.188.TP97, edited by: Letestu, S., Secretariat of the World Meteorological Organization, Geneva, Switzerland, 1966.

Yang, Q., Easter, R. C., Campuzano-Jost, P., Jimenez, J. L., Fast, J. D., Ghan, S. J., Wang, H., Berg, L. K., Barth, M. C., Liu, Y., Shrivastava, M. B., Singh, B., Morrison, H., Fan, J., Ziegler, C. L., Bela, M., Apel, E., Diskin, G. S., Mikoviny, T., and Wisthaler, A.: Aerosol transport and wet scavenging in deep convective clouds: A case study and model evaluation using a multiple passive tracer analysis approach, J. Geophys. Res.-Atmos., 120, 8448–8468, https://doi.org/10.1002/2015jd023647, 2015.

Yu, P., Toon, O. B., Neely, R. R., Martinsson, B. G., and Brenninkmeijer, C. A. M.: Composition and physical properties of the Asian tropopause aerosol layer and the North American tropospheric aerosol layer, Geophys. Res. Lett., 42, 2540–2546, https://doi.org/10.1002/2015gl063181, 2015.

Yu, P., Rosenlof, K. H., Liu, S., Telg, H., Thornberry, T. D., Rollins, A. W., Portmann, R. W., Bai, Z., Ray, E. A., Duan, Y., Pan, L. L., Toon, O. B., Bian, J., and Gao, R.-S.: Efficient transport of tropospheric aerosol into the stratosphere via the Asian summer monsoon anticyclone, P. Natl. Acad. Sci. USA., 114, 6972–6977, https://doi.org/10.1073/pnas.1701170114, 2017.

Yuan, C., Lau, W. K. M., Li, Z., and Cribb, M.: Relationship between Asian monsoon strength and transport of surface aerosols to the Asian tropopause aerosol layer (ATAL): interannual variability and decadal changes, Atmos. Chem. Phys., 19, 1901–1913, https://doi.org/10.5194/acp-19-1901-2019, 2019.
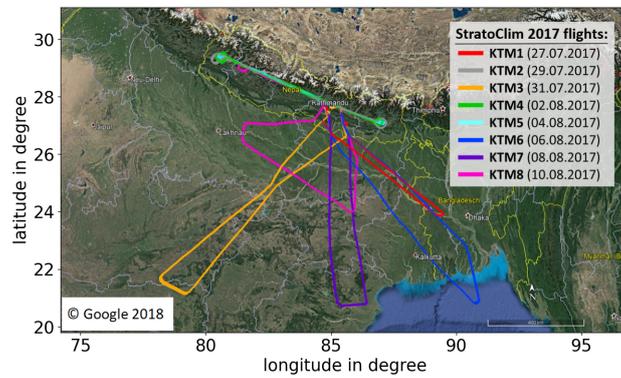
Figure 1. All flight paths of the mission flights conducted in Kathmandu (Nepal) as part of the StratoClim 2017 measurement campaign. GPS data from UCSE, Copyright: © Google 2018.
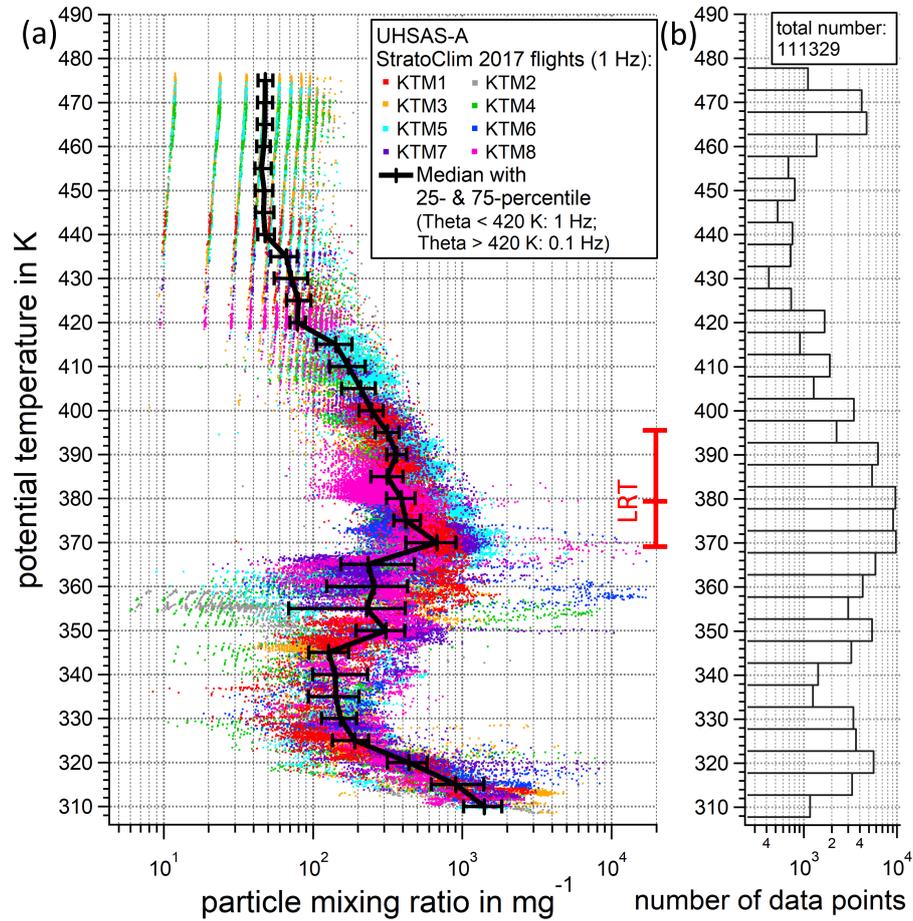
Figure 2. Panel (a): Vertical profile of the particle mixing ratio measured with the UHSAS-A (diameter range: 65 nm - 1 μm) during the StratoClim 2017 measurement campaign, with the potential temperature as vertical coordinate. The 1 Hz resolved data points of the individual measurement flights are marked by individually colored dots. In black the median profile of all flights is plotted in steps of 5 K (each over a ± 2.5 K interval) with the 25 % and 75 % percentiles, based on the 1 Hz data for $\Theta < 420$ K and on the 0.1 Hz data for $\Theta > 420$ K. The red vertical bar indicates the position (minimum, mean, maximum Θ level) of the lapse rate tropopause (LRT; calculated from the ECMWF reanalysis data) during the campaign period. Panel (b): The number of 1 Hz data points included in each 5 K potential temperature interval. Each 1 Hz data point covers a particle size distribution from 65 nm to 1 μm particle diameter.
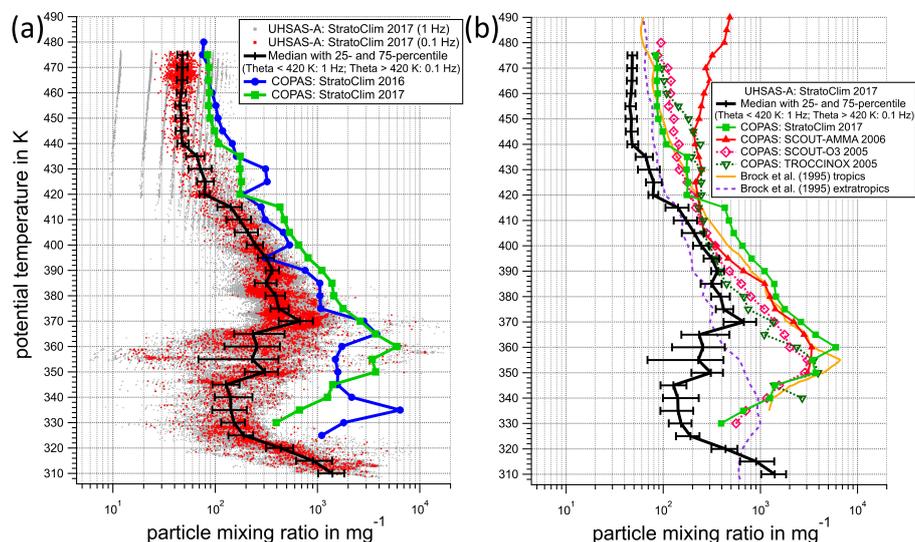
Figure 3. Vertical profile of the particle mixing ratio with the potential temperature as vertical coordinate. Panel (a) shows the 1 Hz resolved particle mixing ratios measured with the UHSAS-A (diameter range: 65 nm - 1 µm) during StratoClim 2017 as gray dots and the 0.1 Hz averaged particle mixing ratios as red dots. In black, the median profile of all flights is plotted in steps of 5 K (each over a $\pm$ 2.5 K interval) with the 25 % and 75 % percentiles, based on the 1 Hz data for $\Theta <$ 420 K and on the 0.1 Hz data for $\Theta >$ 420 K. The median profile of the particle mixing ratio measured by the COPAS (diameter range: 10 nm - 1 µm) during the StratoClim 2016 measurement campaign in the extratropics (Kalamata, Greece) is shown in blue, the profile measured during StratoClim 2017 (Kathmandu, Nepal) in the tropics in green. Panel (b) includes the median profile (with the 25 % and 75 % percentiles) of particle mixing ratios measured with the UHSAS-A during StratoClim 2017 (black line), the median profiles measured by COPAS for particle diameters larger 10 nm during StratoClim 2017 (Nepal, green line), SCOUT-AMMA 2006 (West Africa, red line), SCOUT-O3 2005 (Australia, red dotted line), and for diameter larger 6 nm during TROCCINOX 2005 (Brazil, green dotted line) as depicted in Borrmann et al. (2010). The median profiles, digitized of Fig.1 in Brock et al. (1995), for the tropics are plotted as an orange line and for the extratropics as a dashed purple line.
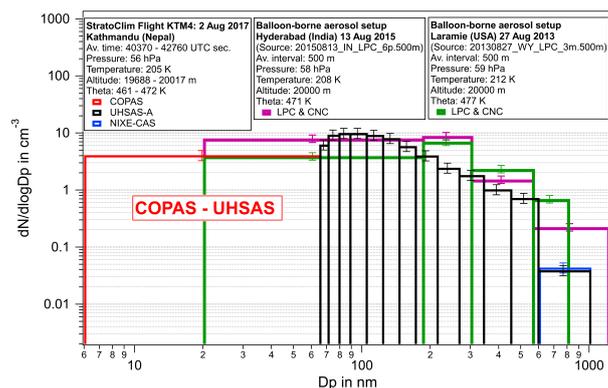
Figure 4. Aerosol particle size distribution combined from the measurements performed by the UHSAS-A, COPAS, and NIXE-CAS (overlapping size range with the UHSAS-A) for the highest flight level reached during the flight KTM4 of the 2017 StratoClim campaign. The particle number concentrations are given for ambient conditions. The concentration of the red marked size bin (6 nm to 65 nm) is the difference of the total number concentrations measured by COPAS (diameter range: 6 nm to 1 μm) and UHSAS-A (diameter range: 65 nm to 1 μm). Air pressure, temperature, altitude, and potential temperature according to the UCSE data set. For comparison, measurements of the balloon-borne measurement set-up described by Ward et al. (2014) and Campbell and Deshler (2014) of flights from Hyderabad (India) and from Laramie (USA) are shown in purple and green, respectively.
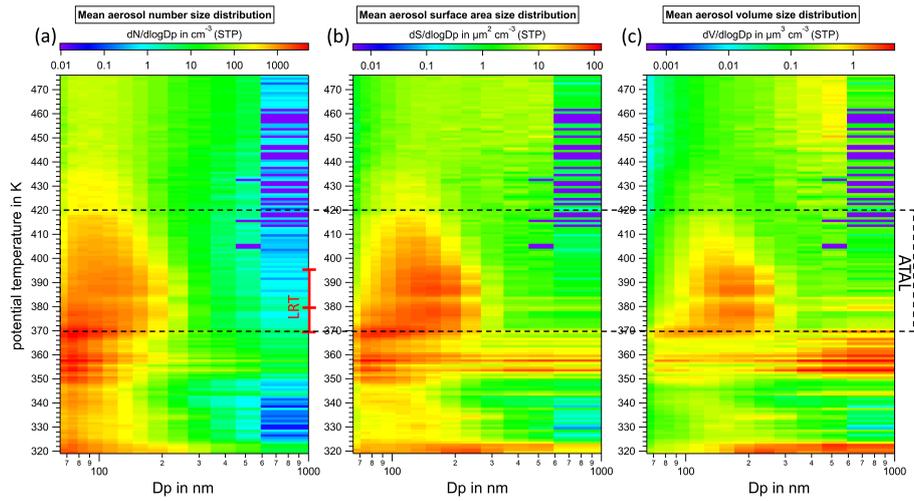
Figure 5. Vertical profile of (a) the aerosol particle number size distribution, (b) the aerosol particle surface area size distribution, and (c) the aerosol particle volume size distribution measured by the UHSAS-A during the 2017 StratoClim field campaign averaged over 1 K potential temperature intervals. The color-coded concentrations for each size-bin are converted from ambient conditions to Standard Temperature and Pressure (STP). The red vertical bar indicates the position (minimum, mean, maximum Θ level) of the lapse rate tropopause (LRT; calculated from the reanalysis data) during the campaign period. The vertical region of the ATAL is indicated with black dashed lines.
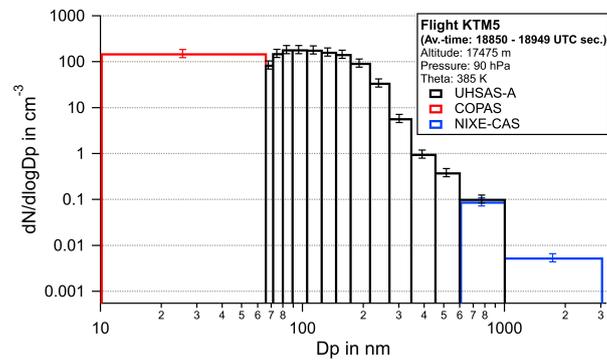
Figure 6. Aerosol particle size distribution measured within the ATAL during flight KTM5 of the 2017 StratoClim measurement campaign. Combined out of the measurements conducted by the COPAS (red size-bin), the UHSAS-A (black size-bins), and the NIXE-CAS (blue size-bins).
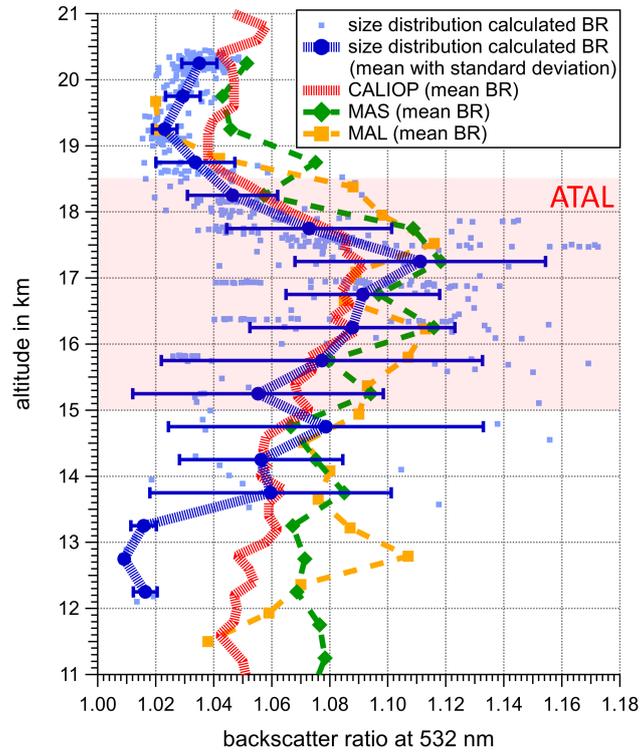
Figure 7. Vertical profile of the backscatter ratio at 532 nm wavelength. Calculated based on the aerosol size distributions measured during the 2017 StratoClim measurement campaign as blue dots (100 s averages) and mean profile (blue line) with standard deviation (blue bars). The mean profiles of the backscatter ratio at 532 nm wavelength measured by CALIOP, MAS, and MAL are plotted in red, green, and orange, respectively.
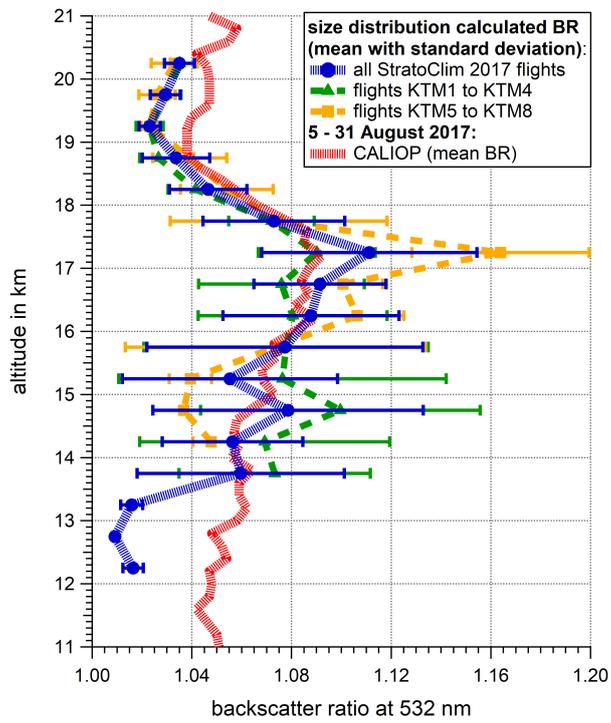
Figure 8. Vertical mean profile of the backscatter ratio at 532 nm wavelength, calculated based on the aerosol size distributions measured during the 2017 StratoClim measurement campaign with the standard deviation as horizontal bars. In blue for the full period of the 2017 StratoClim field campaign, in green for the first half (flights KTM1 to KTM4), and in orange for the second half (flights KTM5 to KTM8) of the campaign period. The red line represents the vertical mean BR profile measured by CALIOP between 5 and 31 August 2017.
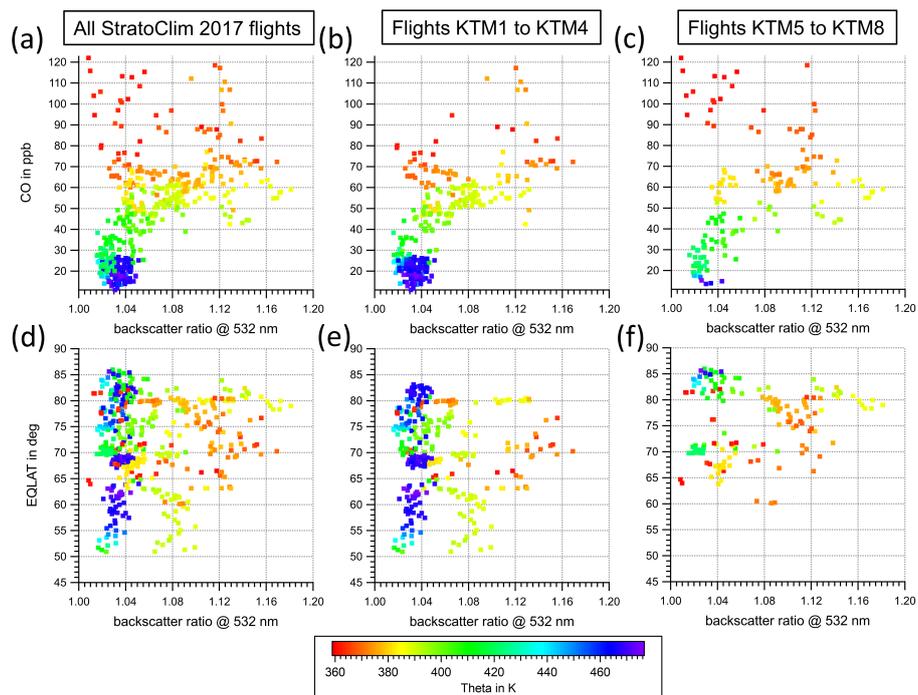
Figure 9. Scatter plots of the size distribution based BR with the CO mixing ratio (panels (a), (b), and (c)) and the AMA-centered equivalent latitude (EQLAT) (panels (d), (e), and (f)). Panels (a), (d) represents the full period of the 2017 StratoClim field campaign, panels (b), (e) the first half (flights KTM1 to KTM4), and panels (c), (f) the second half (flights KTM5 to KTM8) of the campaign period. The potential temperature is color-coded.
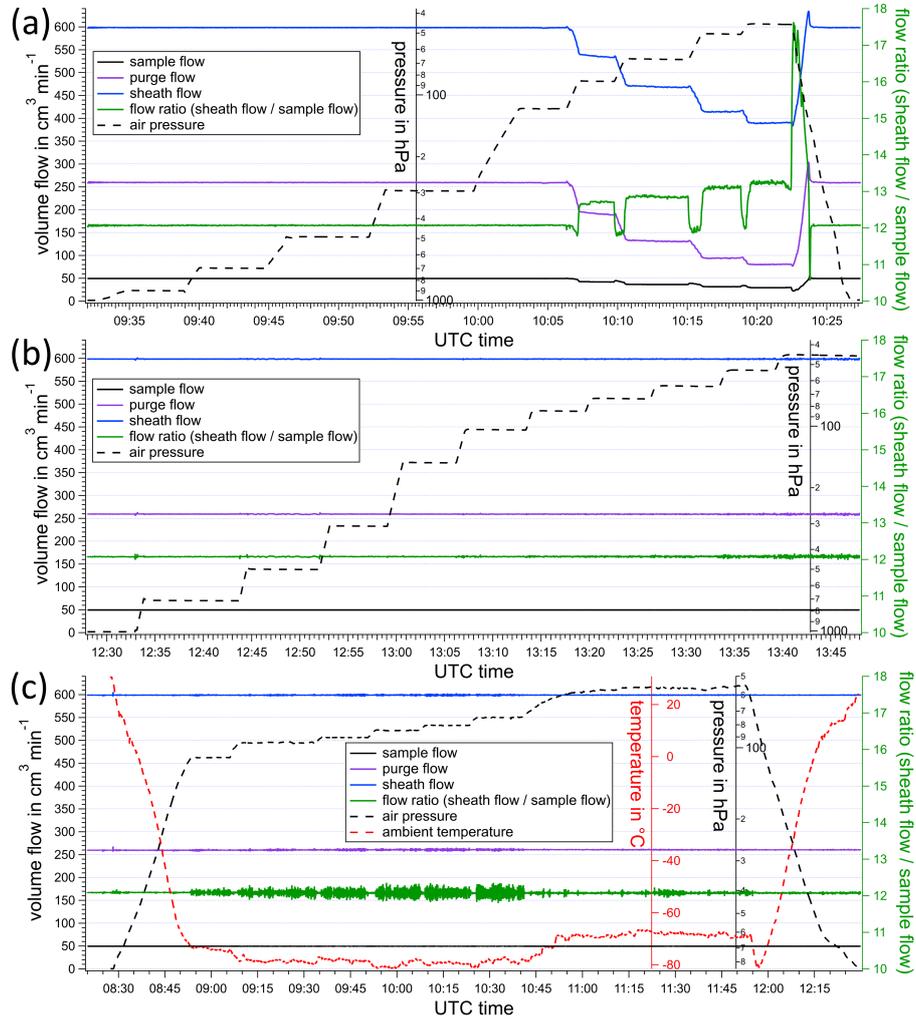
Figure A1. Time series of the UHSAS-A internal flow measurements (sample flow, sheath flow, and purge flow), the ratio between sheath and sample flow, and the air pressure during low pressure chamber tests with the original pump system of the UHSAS-A (panel (a)) and with the new integrated pump system (panel (b)). Panel (c) shows the time series for the StratoClim 2017 flight KTM4 (with the new pump system) also including the ambient static air temperature.
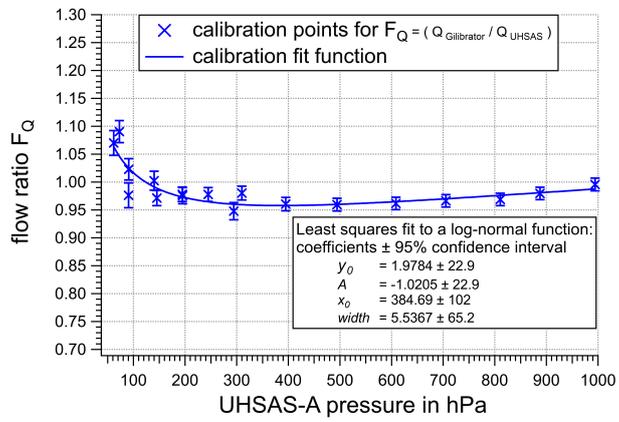
Figure A2. Sample flow characterization measurements as a function of pressure.
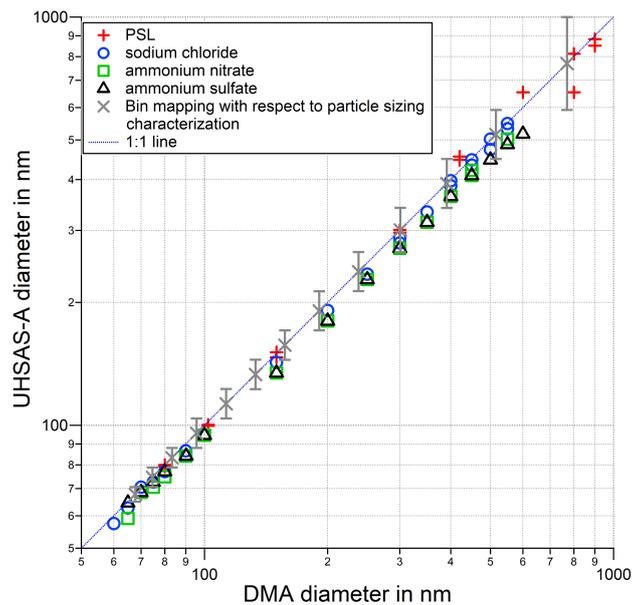
Figure A3. Characterization measurements for the particle sizing of the UHSAS-A: Main particle mode diameter of the size distribution measured by the UHSAS-A (using all 99 available size bins) compared to the particle diameter selected by a DMA for different particle species. The gray bars represent the bin mapping used after the post processing.
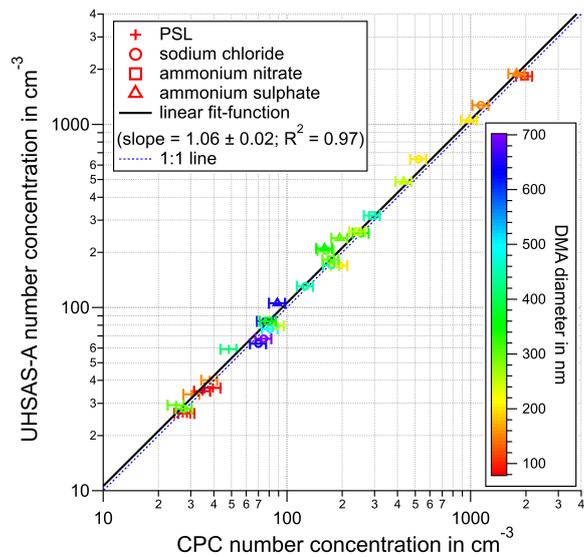
Figure A4. Characterization measurements of the counting efficiency of the UHSAS-A: Comparison of the particle number concentrations measured by the UHSAS-A and the TSI CPC 3025A reference for different particle species and particle sizes (color-coded).
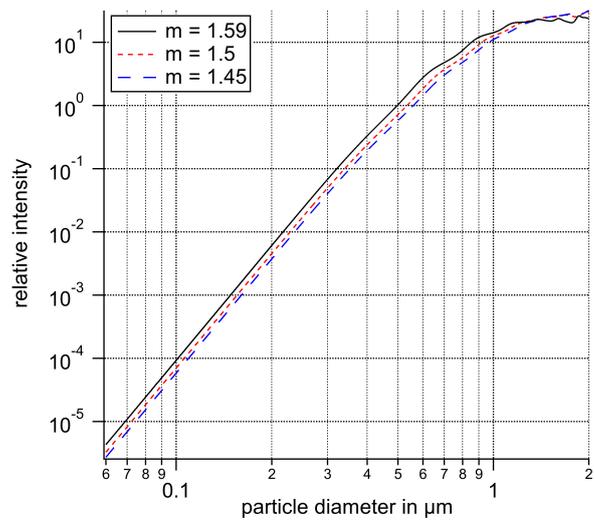
Figure A5. Relative intensity at the detector of UHSAS-A calculated for refractive index of PSL particles (m = 1.59), ATAL aerosol particles (m = 1.5), and stratospheric aerosol particles (m = 1.45).
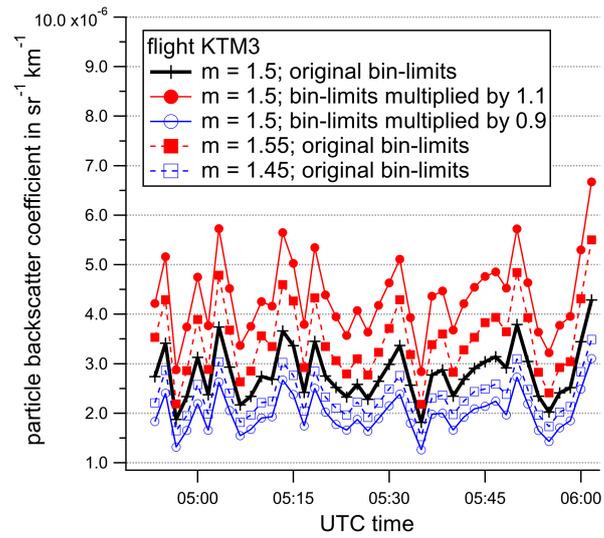
Figure A6. Sensitivity test of the aerosol backscatter coefficient calculation for different refractive indices (m = 1.45, m = 1.5, and m = 1.55) and shifts of the bin-limits of the aerosol size distribution by ± 10 %.
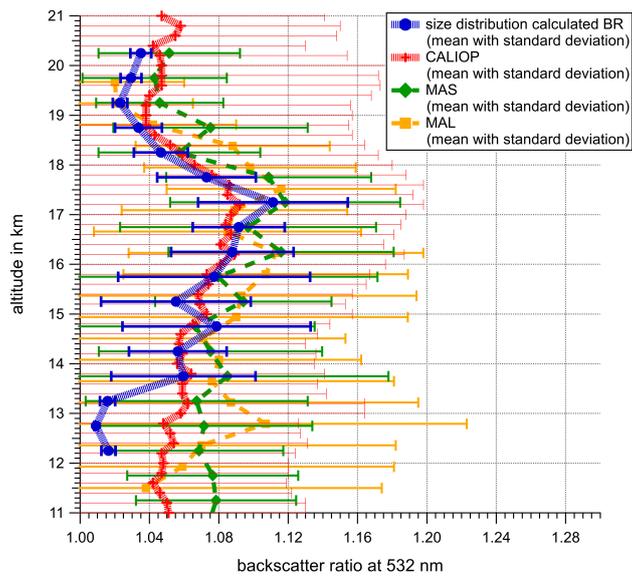
Figure A7. Vertical profile of the backscatter ratio at 532 nm wavelength. Mean profile (blue line) with standard deviation (blue bars) of the calculated BR based on the aerosol size distributions measured during the 2017 StratoClim measurement campaign. The mean profiles (with standard deviation as horizontal bars) of the backscatter ratio at 532 nm wavelength measured by CALIOP, MAS, and MAL are plotted in red, green, and orange, respectively.